MEASUREMENT OF PROTON INTERACTION LENGTH IN THE DSTAU EXPERIMENT AT CERN

A THESIS SUBMITTED TO
THE GRADUATE SCHOOL OF NATURAL AND APPLIED SCIENCES
OF
MIDDLE EAST TECHNICAL UNIVERSITY

BY

NEŞE ERGİN

IN PARTIAL FULFILLMENT OF THE REQUIREMENTS
FOR
THE DEGREE OF MASTER OF SCIENCE
IN
PHYSICS

JANUARY 2025

Approval of the thesis:

MEASUREMENT OF PROTON INTERACTION LENGTH IN THE DSTAU EXPERIMENT AT CERN

submitted by **NEŞE ERGİN** in partial fulfillment of the requirements for the degree of **Master of Science in Physics Department, Middle East Technical University** by,

Prof. Dr. Naci Emre Altun
Dean, Graduate School of **Natural and Applied Sciences** _____

Prof. Dr. Seçkin Kürkcüoğlu
Head of Department, **Physics** _____

Prof. Dr. Ali Murat Güler
Supervisor, **Physics, METU** _____

Examining Committee Members:

Prof. Dr. Bayram Tekin
Physics, METU _____

Prof. Dr. Ali Murat Güler
Physics, METU _____

Assoc. Prof. Dr. Deniz Yılmaz
Physics Engineering, Ankara University _____

Date:03.01.2025

I hereby declare that all information in this document has been obtained and presented in accordance with academic rules and ethical conduct. I also declare that, as required by these rules and conduct, I have fully cited and referenced all material and results that are not original to this work.

Name, Surname: Neşe ERGİN

Signature :

ABSTRACT

MEASUREMENT OF PROTON INTERACTION LENGTH IN THE DSTAU EXPERIMENT AT CERN

ERGİN, Neşe
M.S., Department of Physics
Supervisor: Prof. Dr. Ali Murat Güler

January 2025, 58 pages

The DsTau project at CERN has been proposed to study tau-neutrino production aiming at providing important information for future tau-neutrino measurements. Precise measurement of the tau-neutrino cross section would enable a search for new physics effects in tau-neutrino charged current interactions. The dominant source of tau-neutrino is the sequential decay of D_s mesons produced by proton interactions, whose uncertainty dominates current uncertainty in the tau-neutrino cross section measurement. In this thesis work, the proton interaction length in the tungsten target is measured and the charm pair production in the p-A interactions is studied using the DsTau 2018 pilot run data.

Keywords: DsTau Experiment, Proton Interaction Length, Charmed Decay

ÖZ

CERNDEKİ DSTAU DENEYİNDE PROTON ETKİLEŞİM UZUNLUĞUNUN ÖLÇÜLMESİ

ERGİN, Neşe
Yüksek Lisans, Fizik Bölümü
Tez Yöneticisi: Prof. Dr. Ali Murat Güler

Ocak 2025 , 58 sayfa

CERN'deki DsTau projesi gelecekteki tau-nötrino ölçümlerine önemli bilgiler sağlayacak olan tau-nötrino üretimini çalışmak amacıyla ortaya konuldu. Tau-nötrino tesir kesitinin hassas ölçümü, tau-nötrino yüklü akım etkileşimlerindeki yeni fizik etkilerinin araştırılmasına olanak sağlamaktadır. Proton etkileşimleri sonucunda üretilen D_s mezonlarının sıralı bozunumu tau-nötrinonun baskın kaynağı olmakla birlikte, tau-nötrino tesir kesitinin ölçümündeki belirsizliğin önemli bir kısmı D_s mezonunun ölçümündeki belirsizliğe dayanmaktadır. Bu tez çalışmasında, tungstendeki proton etkileşim uzunluğunun ölçümü ve p-A etkileşimlerinde tılsımlı hadron çifti üretimi, DsTau 2018 pilot deney verileri kullanılarak incelenmektedir.

Anahtar Kelimeler: DsTau Deneyi, Proton Etkileşim Uzunluğu, Tılsımlı Bozunum



To my cats.

ACKNOWLEDGMENTS

I would like to express my sincere gratitude to everyone who has supported me throughout the journey of this thesis. I am deeply grateful to my advisor, Prof. Dr. Ali Murat Güler, for his continuous guidance, expertise, and invaluable feedback throughout this work. To my beloved companion, Emin Yüksel, thank you for your patience, encouragement, and for always finding time for my endless questions. A special thank you to my dear friends Canay Öz, Zozan Sarı, and Elif Güler for their emotional support during my challenging times. I also want to express my gratitude to my sister, Arzu Ergin, for her understanding and support during my stressful times. I would like to thank Dr. Veli Yıldız for allowing me time off from work to focus on this thesis. I am grateful to the entire the DsTau collaboration for their contributions and dedication to the success of this project. Lastly, I would like to acknowledge TENMAK for supporting our project with grant no. 2022TENMAK(CERN)-A5.H3.F2-1, and TÜBİTAK 2210-A Yurt İçi Yüksek Lisans Burs Programı for providing me with financial support throughout my education.

TABLE OF CONTENTS

ABSTRACT v

ÖZ vi

ACKNOWLEDGMENTS viii

TABLE OF CONTENTS ix

LIST OF TABLES xii

LIST OF FIGURES xiii

LIST OF ABBREVIATIONS xvi

CHAPTERS

1 INTRODUCTION 1

2 STANDARD MODEL AND CHARM HADROPRODUCTION 3

2.1 Standart Model of Elementary Particles 3

2.1.1 Composite Particles and Quark Model 6

2.1.1.1 SU(N) Group and Young Tableau 6

2.1.1.2 Mesons in the Quark Model 9

2.1.1.3 Baryons in the Quark Model 11

2.2 Production of Charm Particles 13

3 THE DSTAU EXPERIMENT 15

3.1 Motivation 15

3.2 Methodology 15
3.3 Experimental Setup 16
3.3.1 Nuclear Emulsion 18
3.3.1.1 Development 18
3.3.2 Target Mover 20
3.3.3 Hyper Track Selector 21
4 DATA RECONSTRUCTION 23
4.1 Data Processing 23
4.1.1 Base-track Reconstruction 25
4.1.2 Alignment 26
4.1.3 Tracking 27
4.1.4 Proton Linking 28
4.1.4.1 Proton Selection 28
4.1.4.2 Track Linking 28
4.1.4.3 Segment Linking 29
4.1.5 Vertexing 29
5 MEASUREMENT OF PROTON INTERACTION LENGTH 31
5.1 Proton Interaction Length 31
5.1.1 The Measurement 34
6 CHARM PAIR SEARCH IN THE PILOT RUN DATA 41
6.1 Decay Search 41
6.2 Search For Charmed Hadrons Decaying Into Multi-Prongs 43
6.2.1 Reconstructed vs Truth MC Comparison 45

6.2.2 Decay Search Efficiency Estimation 47

7 CONCLUSION 55

REFERENCES 57

LIST OF TABLES

TABLES

Table 4.1 Overlapping sub-volumes and corresponding folders. 24

Table 5.1 EPOS proton-linking and total efficiencies obtained from linear fit, including errors. 37

Table 5.2 Data proton-linking and total efficiencies obtained from linear fit, including errors. 37

Table 5.3 The number of interacted protons (N) and the number of incoming protons (N0) for each tungsten and their ratios (Data). 38

Table 5.4 The number of interacted protons (N) and the number of incoming protons (N0) for each tungsten and their ratios (EPOS). 38

Table 5.5 Proton interaction length in tungsten as estimated for Data and EPOS. 39

Table 6.1 Reconstruction efficiencies for different cases. 47

Table 6.2 Reconstruction efficiencies for "1 in 1" case. 48

Table 6.3 Reconstruction efficiencies for "2 in 2" case.. 49

LIST OF FIGURES

FIGURES

Figure 2.1 Elementary particles of the Standard Model 4

Figure 2.2 A diagram illustrating the interactions of elementary particles. Lines connect the particles that interact. Photon does not interact with particles beneath the dashed lines (such as the neutrinos and the Z boson)[3]. 5

Figure 2.3 Tensor product of $\mathbf{3}$ representation with $\bar{\mathbf{3}}$ representation (left) decomposes into an octet and singlet (right). 9

Figure 2.4 Weight diagrams for pseudoscalar meson nonet (left), vector meson nonet (right). Horizontal axis is I_z and vertical is hypercharge Y. . . 10

Figure 2.5 Weight diagrams for meson multiplets in SU(4). Pseudoscalar mesons(left), vector mesons (right). 11

Figure 2.6 Weight diagrams for baryon decuplet with spin $\frac{3}{2}$ (left) and baryon octet with spin $\frac{1}{2}$ (right). 12

Figure 2.7 Weight diagrams for baryon multiplets in SU(4). 20_m-plet (right), 20_s-plet (left). 13

Figure 2.8 Feynmann diagrams for first order hadroproduction process. . . . 14

Figure 3.1 D_s kink topology 16

Figure 3.2 Detector Structure in the pilot run. 17

Figure 3.3 On the top, the detector structure used in pilot run with ECC. On the bottom, modified version of it used in physics run. 18

Figure 3.4 The dark room where the development process caried out. 19

Figure 3.5 Visualization of latent image formation and resulting silver grains after development process (top). Microscopic view of charged particle track in emulsion (b). 20

Figure 3.6 The schematic representation of the target mover. 21

Figure 3.7 The schematic representation of the HTS. 22

Figure 4.1 The layout for sub-volumes and sub-areas. 23

Figure 4.2 The layout for overlapping subareas. 25

Figure 4.3 Micro-track reconstruction (left) and base-track reconstruction (right). 26

Figure 4.4 Visualization for the new tracking algorithm. Two tracks come closer and there are possible paths to go from Z1 ato Z2 (a). Using base-tracks, areas are calculated (b). 27

Figure 4.5 The proton track angle distributions in the XZ and YZ planes are displayed, and a Gaussian fit is performed. The primary proton tracks are within the region 3 σ from the fitted curve. 29

Figure 4.6 The proton linking method is visualized, with the upper figure showing the first sub-volume and the lower one illustrating the second sub-volume. 30

Figure 5.1 Interaction probability per unit distance. 31

Figure 5.2 Vertex distribution in beam direction. Vertices inside and outside acceptance cut are shown as red and blue lines respectively. 35

Figure 5.3 EPOS Proton-linking efficiencies as a function of track density. . 36

Figure 5.4 EPOS total efficiencies as a function of track density. 36

Figure 5.5 Comparison of interaction length for Data and EPOS. 39

Figure 6.1 Double charm topology example. 42

Figure 6.2 Flowchart of Charm Matching. 44

Figure 6.3 Difference in X,Y and Z positions for MC truth and reco. 46

Figure 6.4 Efficiency histogram with respect to energy for C_1N_2 topology. . 49

Figure 6.5 Efficiency histogram with respect to energy for C_1N_4 topology. . 50

Figure 6.6 Efficiency histogram with respect to energy for C_3N_2 topology. . 50

Figure 6.7 Efficiency histogram with respect to energy for C_3N_4 topology. . 50

Figure 6.8 Flight length comparison of data and MC for $C_1N_2(N_4)$ topology. 52

Figure 6.9 Flight length comparison of data and MC for $C_3N_2(N_4)$ topology. 52

Figure 6.10 An event with $C_3N_2(N_4)$ topology. 53

Figure 6.11 An event with $C_3N_2(N_4)$ topology through multiple emulsions in the z direction. 53

LIST OF ABBREVIATIONS

DsTau	The DsTau (NA65) Collaboration
DONuT	Direct Observation of Nu-Tau
METU	Middle East Technical University
CERN	The European Organization for Nuclear Research
SPS	Super Proton Synchrotron
SM	Standard Model
CC	Charged Current
ECC	Emulsion Cloud Chamber
MCS	Multiple Coulomb Scattering
TM	Target Mover
HTS	Hyper Track Selector
QCD	Quantum Chromodynamics
MC	Monte Carlo

CHAPTER 1

INTRODUCTION

The "Standard Model" (SM) of particle physics is a profoundly successful yet ironically named framework describing fundamental particles and their interactions. The SM has been confirmed by a series of experiments, including the discovery of the Higgs boson. Even though the SM is a well-established theory, it includes several unexplained phenomena, such as the neutrino mass origins and mass hierarchy of particles. At its foundation, the SM describes the fundamental particles and the forces that govern their interactions: the strong, the weak, and electromagnetic forces. An important aspect of the SM is its generation structure, where quarks and leptons are grouped into three generations. One of the underlying principles in this structure is lepton universality. According to this principle, weak force couples to all leptons in a similar manner. This principle is a cornerstone of the SM's consistency, and any evidence of lepton universality violations could suggest new physics beyond the Standard Model. Lepton universality can be tested by the study of tau neutrino(ν_τ) interactions, and the measurement of ν_τ production is essential for this, as it provides the necessary neutrino flux for interaction experiments. The DsTau (NA65) collaboration at CERN focuses on ν_τ production through D_s meson decays. The primary purpose of this experiment is to measure the differential production cross-section of the D_s meson in proton-nucleus interactions at 400 GeV. A better understanding of D_s meson decays will help reduce uncertainties in ν_τ cross-section measurements and contribute to testing lepton universality.

There are challenges regarding the detection of decay topology, as both the D_s meson and tau lepton have short flight lengths on the order of millimeters and a small kink angle of D_s to tau decay on the order of milliradians. To capture this decay topology

effectively, the DsTau experiment employs an emulsion particle detector, which provides high spatial resolution. Analyzing approximately 2.3×10^8 proton interactions is expected to yield about 10^5 charm decays. A pilot run of the DsTau experiment was conducted in 2018; the emulsion plates from this run are currently undergoing scanning, event reconstruction, and analysis. An initial analysis of a subset of the pilot run data has been performed to estimate the proton interaction length in tungsten which describes the path taken by protons before undergoing hadronic interactions. Moreover, as a result of these high-energy proton interactions, charmed hadrons are produced with distinct topologies. Topology-based charm analysis has been done to estimate charm reconstruction efficiency and the results will be presented in this thesis.

The outline of the thesis is as follows:

- **Chapter 2:** Review of the Standard Model and charm hadroproduction is given.
- **Chapter 3:** The design and operation of the DsTau experiment are described.
- **Chapter 4:** The data structure and analysis methods are explained.
- **Chapter 5:** The results of proton interaction length measurement are presented.
- **Chapter 6:** The decay search efficiency estimations are discussed.
- **Chapter 7:** A summary of the findings from the analysis is given.

CHAPTER 2

STANDARD MODEL AND CHARM HADROPRODUCTION

2.1 Standart Model of Elementary Particles

The particles and their corresponding interactions are well-categorized and studied under the SM of particle physics. The classification of fundamental particles follows from the Spin-Statistics Theorem, which states identical integer spin particles can be in the same quantum state obeying the Bose-Einstein statistics, and those with half-integer spin can not be in the same quantum state obeying Fermi-Dirac statistics and Pauli Exclusion Principle[1]. The particles with integer spin are classified as bosons, which are carriers or mediators of the fundamental forces, while those with half-integer spin are classified as fermions, which are elementary constituents of matter (Figure 2.1). Further, the fermions are divided into two groups:

- Quarks: up(u), down(d), charm(c) strange(s), top(t), bottom(b)
- Leptons: electron(e), muon(μ), tau(τ), electron neutrino(ν_e), muon neutrino(ν_μ), tau neutrino(ν_τ)

and they are organized under three generations based on their masses. Each generation contains two quarks; one up-type(u,c,t) and one down-type quark(d,s,b) and two leptons; one charged lepton(e, μ, τ) and one corresponding neutrino(ν_e, ν_μ, ν_τ) which are neutral leptons. The second and third-generation particles are unstable and decay into the first generation of particles[2]. It is still unknown why matter's constituents exist in this kind of structure.

Mediators transmit fundamental forces between two subatomic particles; when two particles interact, they exchange a mediator, and the mediator transfers momentum

from one to the other. They can be further classified concerning their spin values:

- Odd integer spin ($S = 1$) bosons are photon (γ), $W^{\pm}$, Z^0, and gluons (g).
- Even integer spin bosons are Higgs ($S = 0$) and hypothetical graviton ($S = 2$).

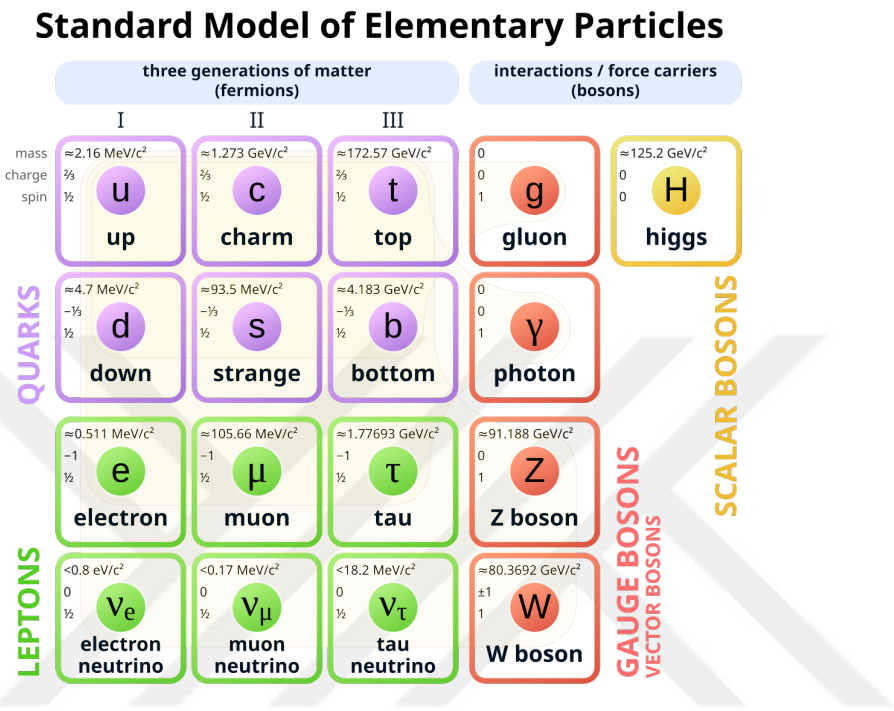


Figure 2.1: Elementary particles of the Standard Model

All known interactions in the universe can be explained by the four fundamental forces, each mediated by one of the bosons above:

- **Gravitation:** Stands for the attractive force between masses. Although its existence has not been confirmed experimentally, the graviton is thought to be the mediator of gravitation. It is the weakest force in terms of strength, yet it has an infinite range.
- **Weak:** Mediated by $W^{\pm}$ or Z^0 bosons. It is extremely short-ranged, operating only at distances of about 10^{-18} meters. As can inferred from the name, it is the weakest after gravitation. Fermions can interact with the weak force, and it causes them to change their "flavour." In other words, the term flavour refers to a type of charge experienced by the weak force.

- **Electromagnetic:** Governs the interactions between electrically charged particles. Mediated by γ, it has an infinite range. Unlike gravity, it can be attractive and repulsive depending on the particle's charge.

- **Strong:** It is shorth-ranged, acting over distances about 10^{-15}meters yet the strongest among all the others. It governs the interactions between particles that have a color charge, such as quarks. Mediated by gluons, and since gluons themselves carry color charge, they can interact with each other. Leptons do not carry color charge; therefore, they do not interact with strong force. Unlike gravity or electromagnetic force, the strength of the strong force increases with increasing distance, creating quark and anti-quark pairs from the vacuum. As a result, individual quarks are never seen in isolation(quark confinement).

As a result of quark confinement, quarks are bound within "hadrons," which are composite particles. Hadrons will be discussed in detail in the upcoming chapter.

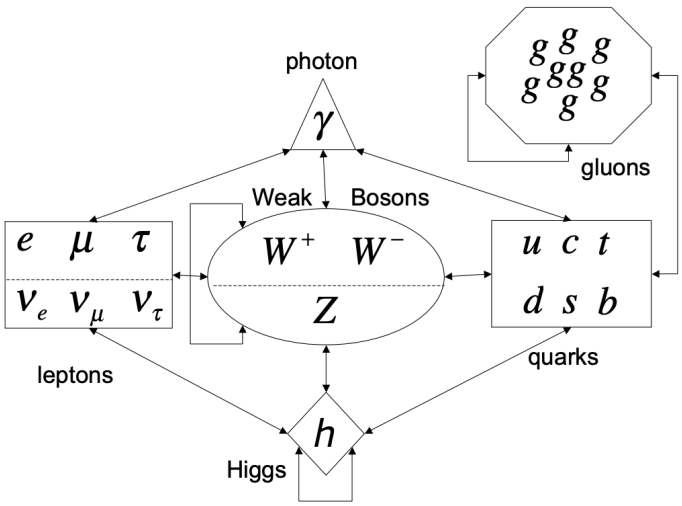


Figure 2.2: A diagram illustrating the interactions of elementary particles. Lines connect the particles that interact. Photon does not interact with particles beneath the dashed lines (such as the neutrinos and the Z boson)[3].

2.1.1 Composite Particles and Quark Model

Until 1950, only a few particles were known[4]. However, with the advent of accelerators, new particles were discovered. The growing number of these particles made it essential to categorize them systematically. The observed spectrum of these particles shows a similar pattern, and this pattern is most effectively explained using the quark model, which forms the basis for understanding strongly interacting composite particles: mesons and baryons.

To elaborate on the quark model, let us consider that there exists N number of quarks, and we need additive internal quantum numbers to distinguish them from each other, such as the third component of Isospin to distinguish the second one from the first one, strangeness to third one from the first two and so on. Therefore, it requires $N-1$ quantum numbers. A special unitary group of degrees N, SU(N), is the most suitable for this model. SU(N) is the group of N by N unitary matrices whose determinants are equal to one. It has N^2-1 generators, and $N-1$ of them can be diagonalized simultaneously. The eigenvalues corresponding to these $N-1$ generators are the additive quantum numbers we mentioned.

2.1.1.1 SU(N) Group and Young Tableau

In SU(N), the fundamental representation is a representation that acts on an N-dimensional complex vector space, and it is denoted by N, while the complex conjugate of the fundamental representation is denoted as $\bar{N}$, which acts on the dual space of N-dimensional vector space. The tensor product representation $N \otimes \bar{N}$ acts on a vector space that is N^2 dimensional, and this tensor product space can be decomposed into irreducible representations(irreps) of the group, which are adjoint representations with dimension equal to dimension of the group [5] i.e N^2-1 and a singlet representation with dimension 1. Young Tableaux, which are basically box diagrams used for representations of groups, help us obtain the dimensions of the irreps if we follow certain rules for constructing them.

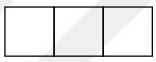
The rules are as follows:

- A row can not be longer than the rows above itself.
- In a row, values inside each box increase from left to right.
- Moving from left to right, no column can be longer than the one before it.
- In a column, values inside each box decrease from top to bottom.

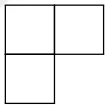
For a configuration dimensionality D is given by :

$$D = \frac{\text{Product of box values}}{\text{Product of hook values}} \tag{2.1}$$

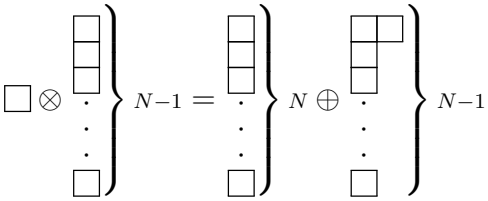
The hook value h is defined for each box as the total number of boxes right and below that box plus the box itself. There are specific configurations we need to consider first:

A totally symmetric configuration: 

A totally anti-symmetric configuration: 

A mixed-symmetric configuration: 

Following the rules, the tensor product of N and $\bar{N}$ gives the legal diagrams as follows:



(2.2)

The first diagram at the RHS of 2.2 is singlet, while the second is adjoint representation. So that we can write:

$$N \otimes \bar{N} = 1 \oplus (N^2 - 1) \tag{2.3}$$

If we want the product of two fundamental representations i.e $N \otimes N$ [6]:

$$\square \otimes \square = \begin{array}{|c|c|}\hline N & N{+}1 \\ \hline \end{array} \oplus \begin{array}{|c|}\hline N \\ \hline N{-}1 \\ \hline \end{array}$$
$$= \frac{N(N+1)}{2\cdot 1} + \frac{N(N-1)}{2\cdot 1} \tag{2.4}$$

for SU(2):

$$2 \otimes 2 = 3 \oplus 1 \tag{2.5}$$

for SU(3):

$$3 \otimes 3 = 6 \oplus 3 \tag{2.6}$$

Now if we want to combine three objects i.e. $N \otimes N \otimes N$, we need to get the product of the result of Eqn. 2.4 with another box:

$$\left(\square\square \oplus \begin{array}{|c|}\hline \\ \hline \\ \hline \end{array}\right) \otimes \square = \left(\square\square\square \oplus \begin{array}{|c|c|}\hline \\ \hline \end{array}\right) \oplus \left(\begin{array}{|c|}\hline \\ \hline \\ \hline \end{array} \oplus \begin{array}{|c|c|}\hline \\ \hline \end{array}\right)$$
$$= \left(\frac{N(N+1)(N+2)}{3\cdot 2\cdot 1} \oplus \frac{(N-1)N(N+1)}{3\cdot 1\cdot 1}\right) \oplus \left(\frac{N(N-1)(N-2)}{3\cdot 2\cdot 1} \oplus \frac{(N-1)N(N+1)}{3\cdot 1\cdot 1}\right) \tag{2.7}$$

Hence

for SU(2):

$$(2 \otimes 2) \otimes 2 = (4 \oplus 2) \oplus 2 \tag{2.8}$$

for SU(3):

$$(3 \otimes 3) \otimes 3 = (10 \oplus 8) \oplus (1 \oplus 8) \tag{2.9}$$

and for SU(4)

$$(4 \otimes 4) \otimes 4 = (20 \oplus 20) \oplus (4 \oplus 20) \tag{2.10}$$

Referring to Eqn. 2.9, the irreps with dimensions 10 (decuplet), 8 (octet), and 1 (singlet) correspond to symmetric, mixed-symmetric, and anti-symmetric configurations, respectively. This classification is evident from the arrangements in Eqn. 2.7. The

same applies to Eqn. 2.10, a symmetric representation has 20 dimensions, and there exist 2 mixed-symmetry representations with a dimension of 20 and a single with a dimension of 4.

2.1.1.2 Mesons in the Quark Model

Mesons consist of one quark q and one anti-quark $\bar{q}$. They are classified with respect to their J^P[7], where J is total angular momentum, P is parity given as:

$$J = L \oplus S \tag{2.11}$$

$$P = (-1)^{L+1} \tag{2.12}$$

Considering only ground state mesons i.e. $L = 0$, J can be either 0 or 1 since q and $\bar{q}$ with spin $\frac{1}{2}$ can combine to be $S = 0$ or $S = 1$.

J^P → $J = 0\,(L = 0, S = 0) \rightarrow 0^-$: pseudoscalar mesons

J^P → $J = 1\,(L = 0, S = 1) \rightarrow 1^-$: vector mesons

Referring to the Eqn. 2.3 for the lightest mesons, i.e. SU(3), we have:

$$3 \otimes \bar{3} = 1 \oplus 8 \tag{2.13}$$

one singlet and an octet. This classification can be visualized in the I_3-Y plane.

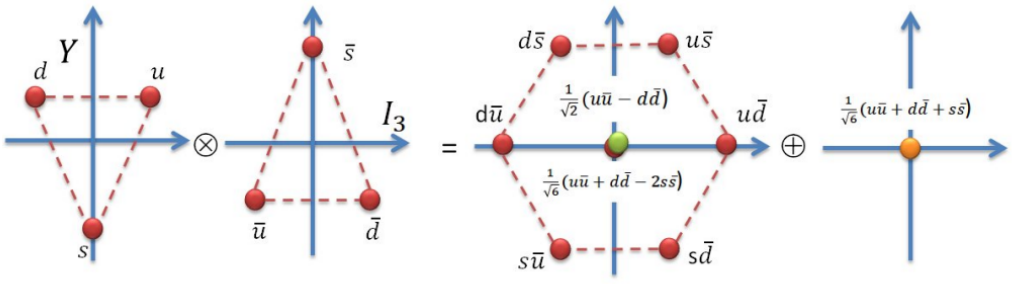


Figure 2.3: Tensor product of $\mathbf{3}$ representation with $\bar{\mathbf{3}}$ representation (left) decomposes into an octet and singlet (right).

As shown in the Figure 2.3, quark and anti-quark triplet combine to form octet states and a singlet state. In total, these states form a nonet, with 9 mesons sharing the same J^P. If $J^P = 0^-$ they are called pseudoscalar mesons while if $J^P = 1^-$ they are called vector mesons.

The eight states of the octet can be transformed into one another through $SU(3)_{flavour}$ symmetry operations. In contrast, the singlet state completely symmetric state and doesn't transform into other states within the octet representation. However, for the pseudoscalar mesons, the states:

$$\eta_1 = \frac{1}{\sqrt{3}}(u\bar{u} + d\bar{d} + s\bar{s}) \tag{2.14}$$

$$\eta_8 = \frac{1}{\sqrt{6}}(u\bar{u} + d\bar{d} - 2s\bar{s}) \tag{2.15}$$

are not observed in nature. The observed states i.e. η and $\eta^{'}$ are the linear combinations of these two states. The same thing applies for the vector mesons: the states with the same quark content of Eqns. 2.14 and 2.15 which are called φ_1 and φ_8 respectively mix to produce experimentally observed ϕ and ω states. In other words, octet and singlet states mix since $SU(3)_{flavour}$ symmetry is broken due to $m_u \approx m_d \neq m_s$. This would not be possible if $SU(3)_{flavour}$ was an exact symmetry. On the other hand, the vector mesons are more massive than their pseudoscalar counterparts although they have the same quark content. The only difference is their spin and the mass difference arises from spin-spin interactions.

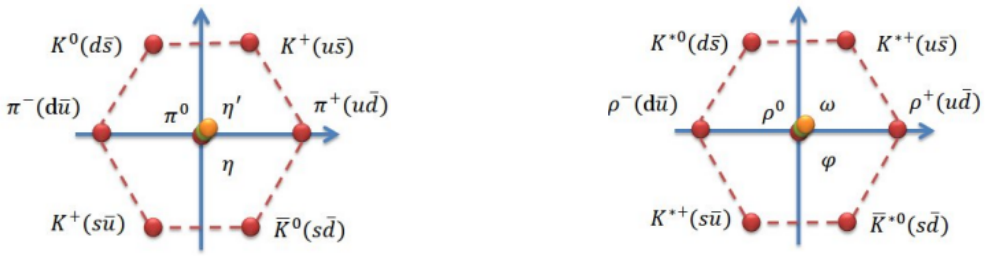


Figure 2.4: Weight diagrams for pseudoscalar meson nonet (left), vector meson nonet (right). Horizontal axis is I_z and vertical is hypercharge Y.

Extending SU(3) to SU(4) from Eqn. 2.3 we have:

$$4 \otimes \bar{4} = 1 \oplus 15 \tag{2.16}$$

in total 16-plet and these mesons can be displayed in a 3D weight diagram with respect to their I_z, Y and charm number C as given in the Figure 2.5 for the pseudoscalar and vector mesons separately. The middle plane represents SU(3) mesons with zero charm, while the mesons in the upper plane have a charm of +1, and those in the lower plane have a charm of -1. $SU(4)_{flavour}$ symmetry is even more broken than $SU(3)_{flavour}$ symmetry because the charm quark is more massive than the strange quark. As a result, the 15-plet and singlet states mix into 16 mesons, as in the case for SU(3).

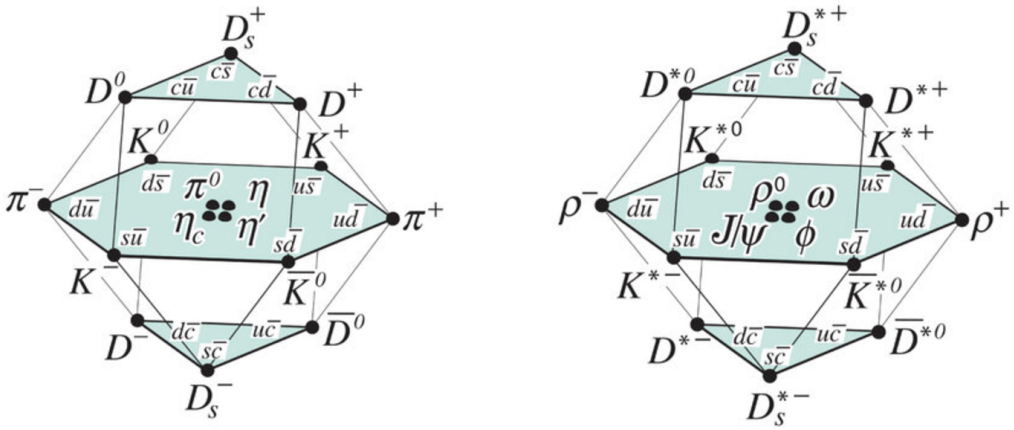


Figure 2.5: Weight diagrams for meson multiplets in SU(4). Pseudoscalar mesons(left), vector mesons (right).

2.1.1.3 Baryons in the Quark Model

To explain the observed baryon spectrum, we need to consider the overall symmetry of quark wavefunction rather than $SU(N)_{flavour}$ symmetry. The total wavefunction is:

$$\Psi_{tot} = \psi_{space}\phi_{flavour}\chi_{spin}\xi_{color} \tag{2.17}$$

and it must be anti-symmetric since a baryon is a system of identical fermions contains three quarks, and therefore, they obey Fermi-Dirac statistics. The color wavefunction part is also anti-symmetric due to color confinement, which states that no color-charged particle can exist in isolation. For baryons in ground state (i.e L = 0) space wavefunction is symmetric i.e $P = (-1)^L = +1$. Overall, ground-state baryons can only be constructed from totally symmetric combinations of flavour and spin wavefunctions[8]. For a baryon, the total spin can be $\frac{1}{2}$, and the spin state in this case is mixed symmetric or $\frac{3}{2}$ with a totally symmetric state. Thus, for the lightest baryons, we need to combine symmetric decuplet with symmetric $\frac{3}{2}$ spin state and mixed symmetric octet with mixed symmetric $\frac{1}{2}$ spin state. As a result we have decuplet of spin-$\frac{3}{2}$ and octet of spin-$\frac{1}{2}$ baryons as given in the Figure 2.6.

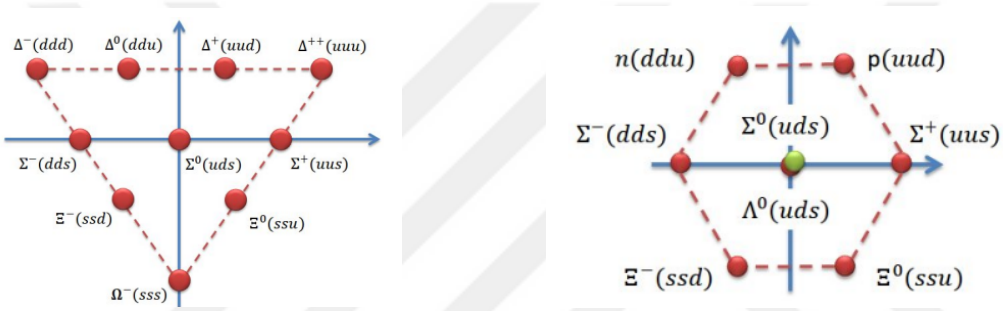


Figure 2.6: Weight diagrams for baryon decuplet with spin $\frac{3}{2}$ (left) and baryon octet with spin $\frac{1}{2}$ (right).

Suppose we add charm quark and extend $SU(3)_{flavour}$ to $SU(4)_{flavour}$, as explained previously. In that case, we can only combine symmetric i.e. 20_s multiplets with symmetric spin-$\frac{3}{2}$ states and mixed symmetric i.e. 20_m multiplets with mixed-symmetric spin-$\frac{1}{2}$ states. Note that, in the Figure 2.7 the bottom level of 20_m-plet is charmless SU(3) baryon octet while the bottom level of 20_s-plet is charmless SU(3) baryon decuplet.

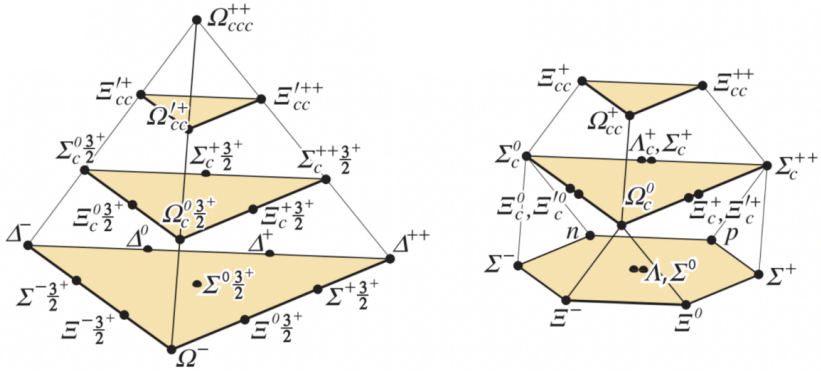


Figure 2.7: Weight diagrams for baryon multiplets in SU(4). 20_m-plet (right), 20_s-plet (left).

2.2 Production of Charm Particles

In high energy hadron-hadron collisions (e.g. p-p, p-A, A-A), the energy involved is sufficient to produce new particles, including charm quarks. The production mechanism referred as "charm hadroproduction" [9] is explained by Parton Model. In the Parton Model framework, the hadron is modeled as a distribution of partons i.e quarks and gluons. Thus, when two hadrons collide , it can be thought of as the partons inside interact each other strongly. This interaction process is explained by Quantum Chromodynamics(QCD). Interaction of two partons can occur at leading-order by gluon-gluon fusion or quark-antiquark annihilation, both are first-order process and resulting in charm-anticharm pair as shown in Figure 2.8. Once the charm quark pair is produced, since the quarks can not exist in isolation they hadronize. In other words, they form bound states with other quarks and result in hadrons.

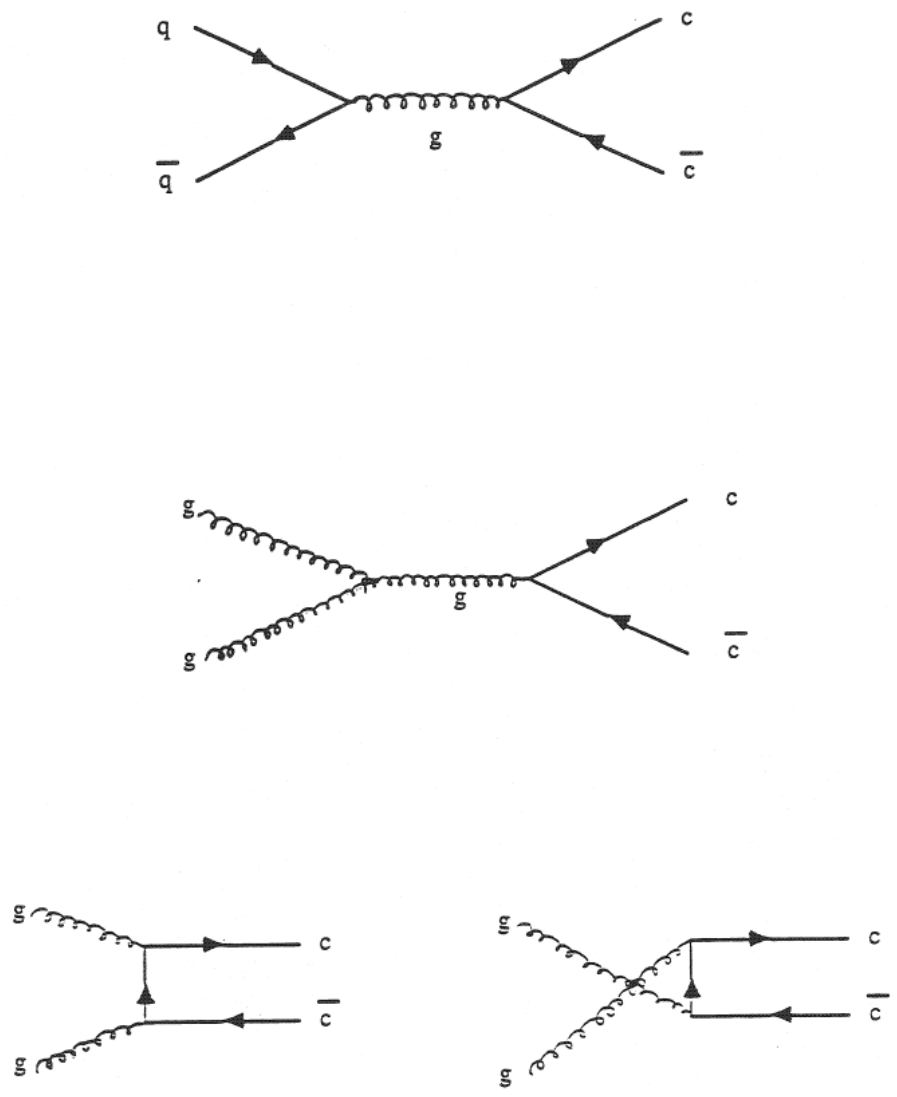


Figure 2.8: Feynmann diagrams for first order hadroproduction process.

CHAPTER 3

THE DSTAU EXPERIMENT

3.1 Motivation

The DsTau experiment is designed to investigate the production of D_s meson and its subsequent decays into τ lepton and ν_τ neutrino in 400 GeV p-A collisions. The primary objective is to measure the differential production cross-section of D_s meson by analyzing approximately 2.3×10^8 p-A interactions out of 4.6×10^9 proton on target(p.o.t) and detecting around 1000 D_s to τ decays[10]. A precise measurement of D_s differential production cross-section so that the decay rate will give precise ν_τ flux that can be used in ν_τ charged current interaction experiments. ν_τ CC cross section is measured in the DONUT experiment[11] for the first time, and they used ν_τ, which are the result of charmed hadron decays of high energy proton interactions. However, the main objective was not measuring the ν_τ flux. Instead, it was to detect ν_τ interactions and observe τ leptons produced in these interactions. They were able to observe only 9 ν_τ interactions, and due to a limited number of observed events, the systematic uncertainty was huge, more than 50% as a result of ν_τ flux uncertainty. By predicting the ν_τ flux, the DsTau experiment will reduce systematic uncertainty to $\approx 10\%$ in the future ν_τ experiments.

3.2 Methodology

The primary source of ν_τ are $D_s^\pm$ which are produced in p-A interactions. As given in Eqn. 3.1 the leptonic decay of D_s into τ and ν_τ, further the decay of τ into in another ν_τ and a hadron gives the so-called double-kink topology as shown in Figure. 3.1

$$D_s^+ \to \nu_\tau + \tau^+ \to X + \bar{\nu}_\tau$$
$$D_s^- \to \bar{\nu}_\tau + \tau^- \to X + \nu_\tau \tag{3.1}$$

In addition, due to charm number conservation, there will be another charmed particle produced alongside $D_s^\pm$ such as $D^\pm/D^0$. The double kink topology, along with having a charmed partner, are the main indicators for the presence of D_s.

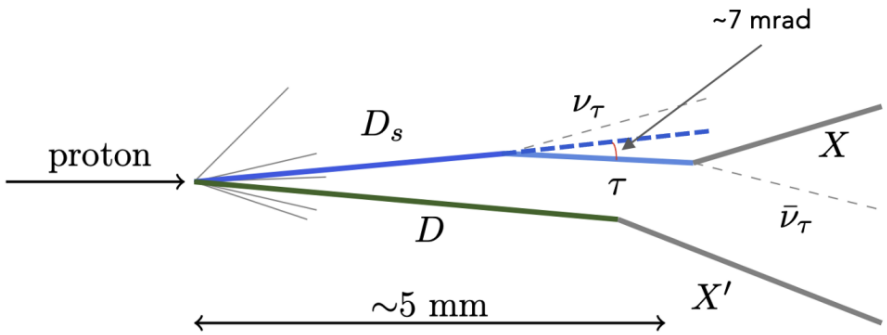


Figure 3.1: D_s kink topology

However, there are technical challenges regarding D_s detection. The flight lengths of both decays are quite small: 3.3 mm for D_s and 2.0 mm for τ in addition to small kink angle of D_s which is approximately 7 mrad. Therefore, to detect such a small angle, a high-resolution detector, namely a nuclear emulsion, is used for tracking.

3.3 Experimental Setup

The experiment uses fixed-target setup. In the setup, to serve as an interaction medium, tungsten is used; for particle track detection, emulsion films are employed; and for the decay volume, plastic is used.

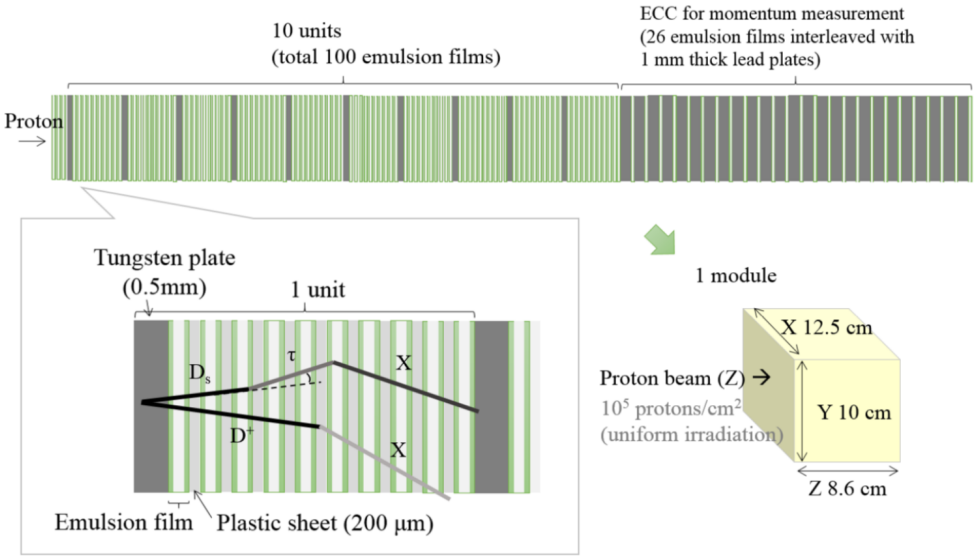


Figure 3.2: Detector Structure in the pilot run.

The pilot run setup consists of two parts. The first part has 10 units, each unit having two 500 μm-thick tungsten and ten 320 μm-thick emulsion films in between. In addition, 5 emulsions placed at the beginning of the first unit which acts as veto plane for incoming protons. These 10 units with the addition of 5 emulsions is called a module. The size of the module is 12.5 cm $\times$ 10 cm. The second part, the Emulsion Cloud Chamber (ECC), contains 25 lead plates each having 1000 μm thickness, interspersed with 26 emulsions as shown in the Figure 3.2. The purpose of the ECC is to measure momentum of particles using the Multiple Coulomb Scattering (MCS).

For physics run in 2021, ECC part is modified due to high track density resulting from electromagnetic showers. Instead of lead, 3 tungsten plates with 25 emulsion films in between are used as shown in the Figure 3.3. Also, in order to increase vertex reconstruction, the size of module is increased to 25 cm $\times$ 20 cm.

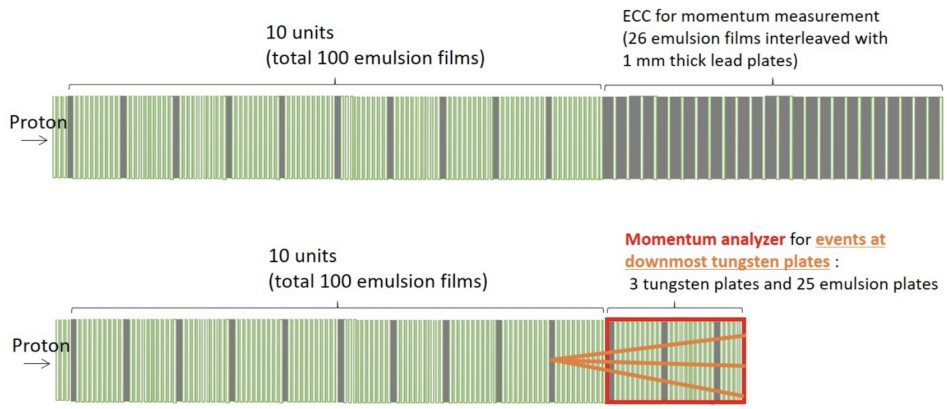


Figure 3.3: On the top, the detector structure used in pilot run with ECC. On the bottom, modified version of it used in physics run.

3.3.1 Nuclear Emulsion

A nuclear emulsion film consists of silver halide, most commonly silver bromide(AgBr) crystals suspended in gelatin. There are impurities introduced into the crystal called as "sensitization centers" and they act as electron traps since they are positively charged. When a charged particle passes through the crystal, it imparts energy to the valence band electrons and these electrons jumps to the conduction band. In order to electrons to move from valence band to conduction band, 2.684 eV energy is needed for (AgBr) crystals. These excited electrons are trapped by sensitization centers and as a result the center becomes negatively charged and attracts silver ions within the crystal lattice. Trapped electron and silver ion combine and produce silver atom ($Ag^+ + e^- \rightarrow Ag$). This process repeats and lead to formation of small aggregates of silver atoms (Ag_n, where $n \geq 4$). When the aggregate becomes large enough i.e Ag_4) a stable structure called "latent image center" is formed[12].

3.3.1.1 Development

Produced latent images are not visible under the microscope. In order to make them visible, development process is needed. The whole development process is carried

out in the dark room(Figure 3.4) in order to prevent damage to particle tracks formed. During development, latent images amplified chemically and the steps are as follows:

- **Immersion in Developer Solution:** The emulsion is immersed in developer solution. The reducing agents from the developer solution donate electrons to the latent image centers and reduce the silver ions to silver atoms. Therefore, more AgBr crystals converted into metallic silver which leads to formation of visible silver grains.
- **Stopping:** The emulsion is immersed in stop bath which prevents further reduction of silver ions.
- **Fixing:** The emulsion is immersed in fixer solution. The fixer removes crystals that do not have a latent image center. After fixing, the emulsions can be exposed to light.
- **Washing:** The emulsion is washed with water so that there are any residual chemicals from the previous processes left which could effect the image quality.



Figure 3.4: The dark room where the development process caried out.

When development process is done, emulsion films are ready to be scanned.

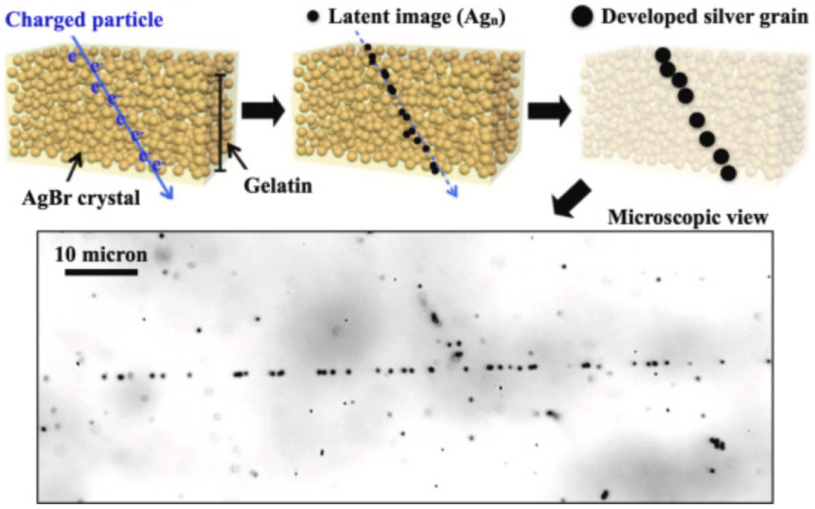


Figure 3.5: Visualization of latent image formation and resulting silver grains after development process (top). Microscopic view of charged particle track in emulsion (b).

3.3.2 Target Mover

Irradiation of the entire emulsion film at once is not feasible due to limited spot size of proton beam which is about 10 mm. Additionally, concentrating the proton beam on a limited area results in a high track density, which compromises the accuracy of track analysis in return. To overcome these issues and ensure uniform irradiation across the entire surface of the emulsion film, a Target Mover(TM)[13] system is used. The TM moves the emulsion module in X and Y axis in a controlled manner with respect to beam which has 10^5 protons per spill in 4 seconds interval. To ensure uniform proton density, the Y step is set based on the proton beam size. The X step is calculated based on proton density and intensity. In the 2016 test run, beam density variations in the X direction led to errors, so in 2017, a scintillator counter was added to monitor intensity, allowing better control of the target mover speed and resulting in more uniform proton distribution. A small-scale TM prototype was tested in 2016, 2017, and used during the 2018 pilot run. For the 2021 physics run, the detector modules were four times larger, requiring a new TM capable of handling a 20 kg payload. The

new TM design, included enhanced features to move the stage at a speed proportional to the beam intensity, optimized for the DsTau experiment.

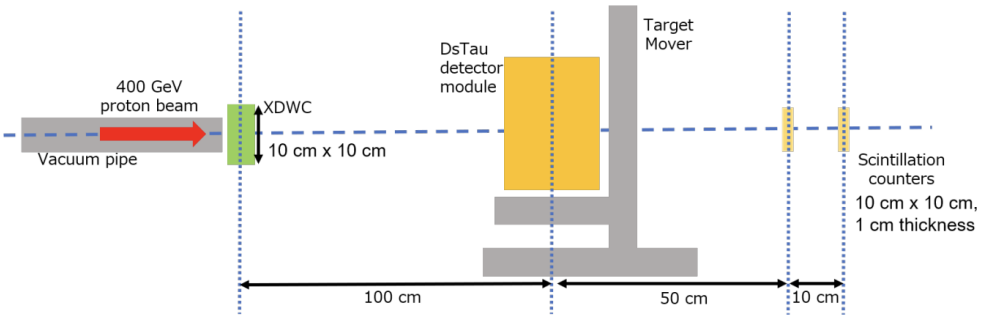


Figure 3.6: The schematic representation of the target mover.

3.3.3 Hyper Track Selector

The Hyper Track Selector (HTS) is an automated system employed for the scanning of emulsion films. It is utilized in a range of experiments that require emulsion-based detection and analysis. The HTS operates at an scanning speed of $5000\,\mathrm{cm}^2$ per hour, enabling rapid processing of emulsion films.

The HTS scans the emulsions at different depths by adjusting focal length of the imaging lens, collects tomographic images, and digitizes each image in grey scale. Then, these digitized images are sent to computers for track recognition, where individual pixels are analyzed to detect clusters of grains corresponding to particle tracks. The clusters in different layers of the emulsion are linked, and micro-tracks are reconstructed as a result[14].

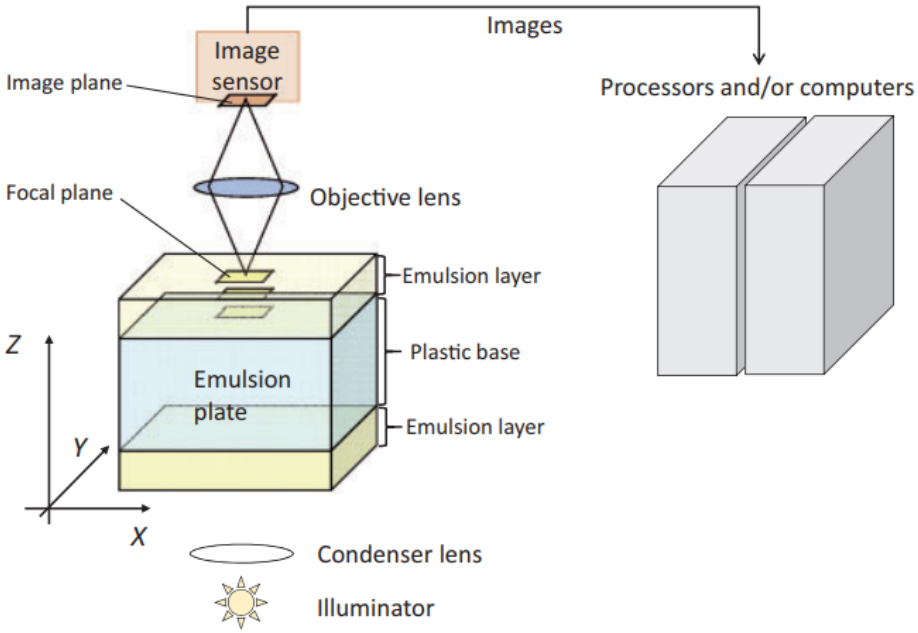


Figure 3.7: The schematic representation of the HTS.

CHAPTER 4

DATA RECONSTRUCTION

4.1 Data Processing

A pilot run was conducted in 2018, and 30 modules were exposed to proton beam. Each module contains 105 emulsion films with a $125 \times 100\,\mathrm{mm}^2$ area. A module is subdivided into sections to handle the large dataset produced as shown in the Figure 4.1, allowing computers to process data faster. The division is as follows:

- The whole module is divided into eight volumes.
- Each volume is divided into 63 subareas.

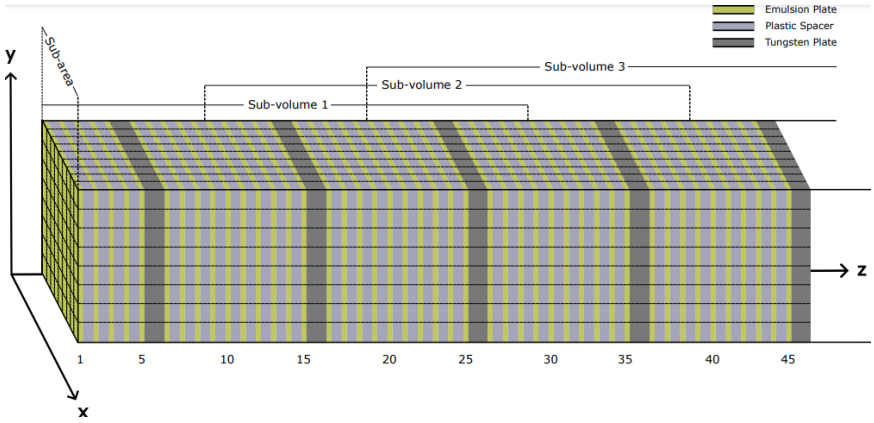


Figure 4.1: The layout for sub-volumes and sub-areas.

These eight volumes or sub-volumes overlap as shown in Table 4.1. This overlap is designed to ensure continuous tracking of particles.

Volume	Start Plate	End Plate	Folder Name
1	1	30	pl001_030
2	11	40	pl011_040
3	21	50	pl021_050
4	31	60	pl031_060
5	41	70	pl041_070
6	51	80	pl051_080
7	61	90	pl061_090
8	71	105	pl071_105

Table 4.1: Overlapping sub-volumes and corresponding folders.

In each sub-volume, there are three tungsten and 30 emulsion films, and due to 5 additional emulsion films at the beginning of the module, the last sub-volume contains 35 emulsion films. Again, the division for the sub-areas is designed in a way that each area overlaps. Due to the alignment or nature of the scanning setup, the position of the emulsion can vary by about ±3 mm. To account for this variation, a rectangle with $135 \times 105\,\mathrm{mm}^2$ area is divided into nine rows and seven columns of smaller squares, each having a size of $15 \times 15\,\mathrm{mm}^2$ and they are referred to as "main parts." Further, the size of these squares increased by 1 mm in each direction, having a size of $17 \times 17\,\mathrm{mm}^2$ as a result and referred to as "full parts," which ensures that the sub-areas overlap as shown in Figure 4.2[15]. This ensures continuous tracking without missing any track or creating gaps in the analysis.

In the DsTau experiment, the data processing starts with micro-tracks and continues with:

- Base-track reconstruction
- Alignment
- Volume-track reconstruction
- Proton-linking
- Vertex reconstruction
- Decay search

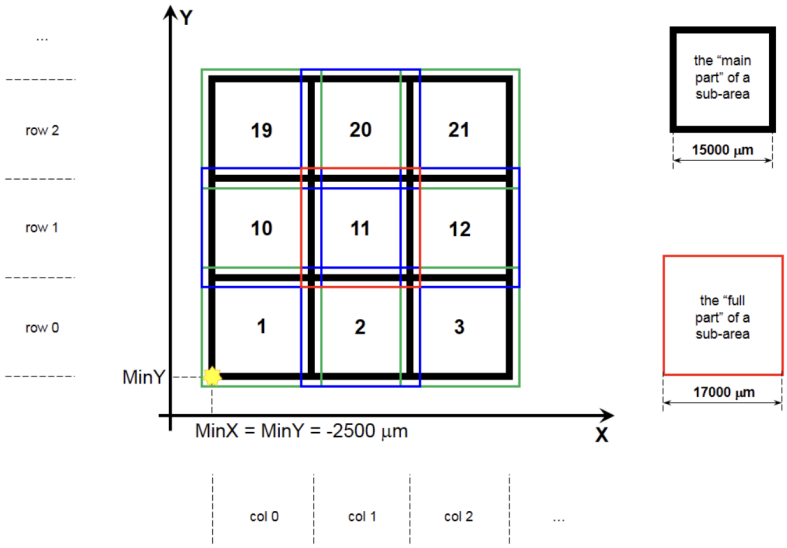


Figure 4.2: The layout for overlapping subareas.

4.1.1 Base-track Reconstruction

Each emulsion film has two active layers separated by a plastic base. In order to reconstruct the entire particle trajectory in an emulsion film, the first step is to link micro-tracks. If two micro-tracks from the bottom and top layers are spatially close in and their angles are aligned within a small tolerance, they are linked by a linear path across the plastic base. This linear path's intersection with the plastic base's midpoint (in z-direction) is selected as the segment point. The position x, y, and z values of this segment, along with the slope of the linear path in xz and yz planes, are used to form "base-tracks" (as shown in the right side of Figure 4.3). The position and slope information for each base-track:

$$\vec{R} = (x, y, z) \qquad \vec{V} = (\tan\theta_x, \tan\theta_y, 1)$$

are defined with respect to local reference frame of each emulsion film.

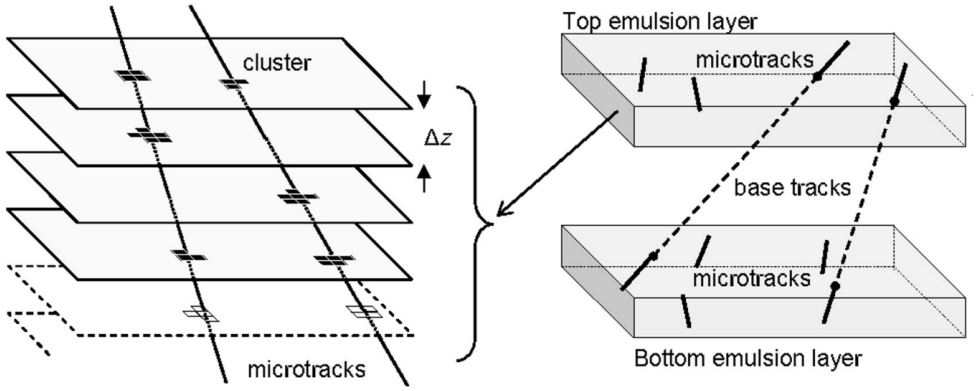


Figure 4.3: Micro-track reconstruction (left) and base-track reconstruction (right).

4.1.2 Alignment

Stacking emulsion films together into a module can not be done perfectly, and this causes positional and rotational shifts relative to one another. As a result, their local reference frames may not match. To correct misalignments between individual films in a module, alignment is required. In the alignment process, affine transformation:

$$\begin{bmatrix} x' \\ y' \end{bmatrix} = \begin{bmatrix} a & b \\ c & d \end{bmatrix} \begin{bmatrix} x \\ y \end{bmatrix} + \begin{bmatrix} e \\ f \end{bmatrix}$$

where:

- (x, y) are the coordinates in the original local reference frame
- (x', y') are the coordinates in the transformed global reference frame
- a, b, c, d define rotation and deformation transformations
- e, f represent translations in the x and y directions

is applied film-to-film. In other words, one film is chosen as global, and the one follows it as a local reference frame. The beam protons are ideal for calculating affine transformation parameters since they are nearly perpendicular to the surface of

the emulsion, and due to that, their transverse positions remain consistent across all the films. Once the parameters corresponding to transformation between 2 films are found using these proton tracks, the transformation is applied for all the tracks in the film referred to as local. This procedure continues until each film is aligned.

4.1.3 Tracking

Tracking refers to the process of connecting base-tracks from consecutive emulsion films. Tracking algorithms, such as the one used in the OPERA, do not work effectively in the DsTau experiment due to higher track density in a smaller angular space. To overcome this issue, a new tracking algorithm is created as shown in Figure 4.4.

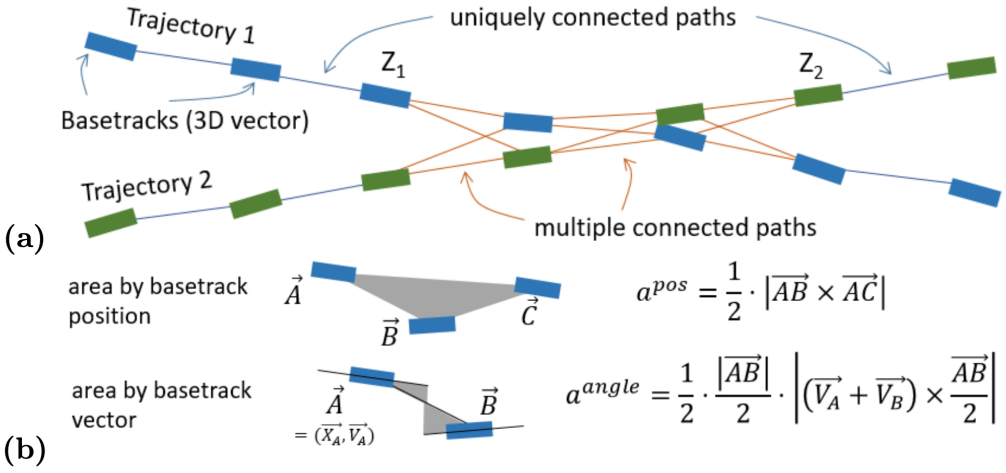


Figure 4.4: Visualization for the new tracking algorithm. Two tracks come closer and there are possible paths to go from Z1 ato Z2 (a). Using base-tracks, areas are calculated (b).

Considering the Figure 4.4, between Z_1 and Z_2 there are 4 base-tracks resulting in $2^4 = 16$ possible connection paths. The algorithm calculates area using positions of 3 base-tracks i.e. a^{pos} and another area using vectors of 2 base-tracks i.e. a^{angle} for each path. Then it takes avarage using the formula:

$$a^{\text{avarage}} = (\sum_{i}^{n-2} a^{\text{pos}} + \sum_{i}^{n-1} a^{\text{angle}})/(n - 0.5) \tag{4.1}$$

The right path is the one which has the smallest a^{avarage}.

4.1.4 Proton Linking

Normally, proton tracks can be selected in anywhere the module by checking if a track has segments in the first 5 emulsion plates. However, since the module is divided into sub-volumes, the analysis of tracks is localized to each specific volume making it difficult to determine the origin of the tracks. Additionally, a track may continue through several sub-volumes, but due to the division, they are treated as separate entities. To tackle these challenges proton-linking algorithm[16][17] is developed and we can select protons and follow them until the end of the module. There are 3 main steps in the process:

- Proton Selection: Recognizes and selects the primary protons within the data.
- Track Linking: Links proton tracks that extend across multiple sub-volumes.
- Segment Linking: Maintains the continuity of track segments across sub-volumes, reconstructing the complete particle trajectories.

4.1.4.1 Proton Selection

First, tracks having at least 3 segments in the first 5 emulsion plates are chosen. Second, linear fit is applied to the segments of each track to find slopes of tracks. Then Gaussian fit is applied to these slopes (Figure 4.5). Proton tracks are selected if their angles are within 3 sigma of the resolution.

4.1.4.2 Track Linking

Tracks identified as proton are traced using a unique parameter called "TrackID". In a sub-volume, TrackID is unique for each track. As mentioned before, there are 3 tungstens in each sub-volume. To process, the first 5 emulsions before the first tungsten are considered as downstream, and the other 5 emulsions before the second tungsten as upstream. Two vectors are created for each section containing unique

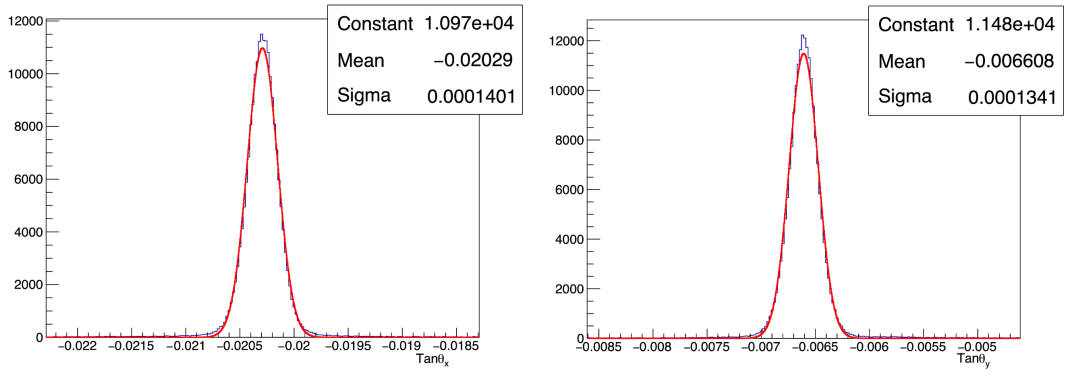


Figure 4.5: The proton track angle distributions in the XZ and YZ planes are displayed, and a Gaussian fit is performed. The primary proton tracks are within the region 3 σ from the fitted curve.

TrackIDs and they are compared with each other. If a TrackID is not found in the downstream while it is in the upstream, this means the track is interacted.

4.1.4.3 Segment Linking

Although TrackIDs are unique in a sub-volume, the TrackIDs for identical tracks vary between neighboring sub-volumes. Thus it can not be used for tracking between sub-volumes. However, a unique parameter called "SegmentID" assigned to each emulsion plate can be used for tracking between neighboring sub-volumes. As shown in Figure 4.6, neighboring sub-volumes overlap; for example, the upstream part of the first sub-volume is regarded as downstream of the second sub-volume and has the same emulsion plates, so the same SegmentID. Linking these segments, we can link the tracks in subsequent sub-volumes.

Applying track linking and segment linking through all the sub-volumes, all protons tracks are linked through the module.

4.1.5 Vertexing

This process is independent from proton linking and is done using the volume-tracks. Using the tracks that stop or start inside the module, the vertexing is performed.

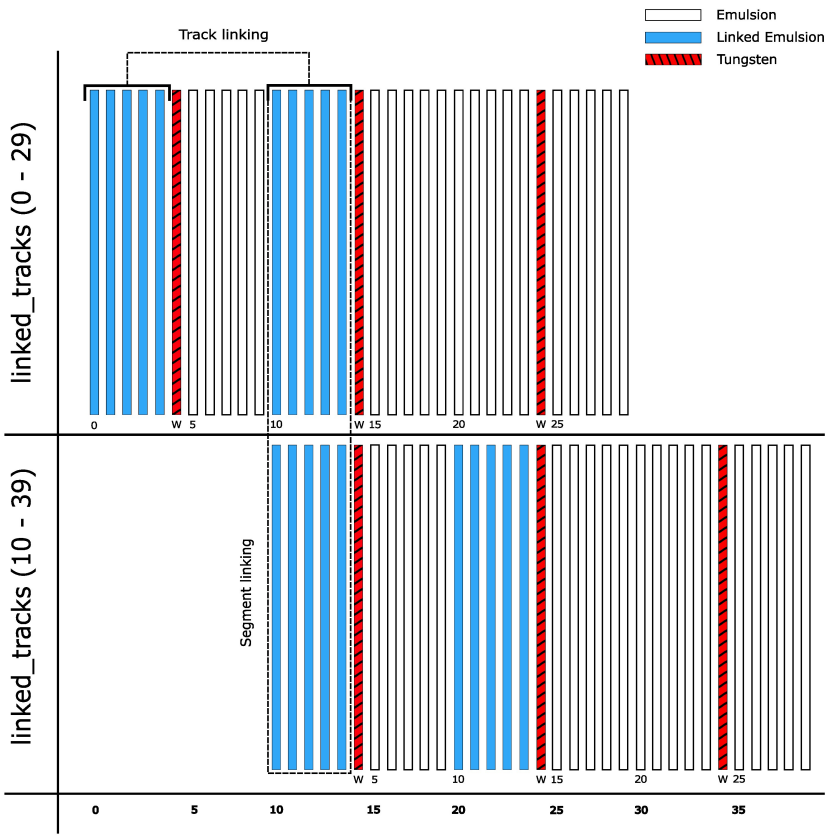


Figure 4.6: The proton linking method is visualized, with the upper figure showing the first sub-volume and the lower one illustrating the second sub-volume.

Tracks having at least 3 segments and angle $\tan\theta < 0.4$ are used for vertex reconstruction. Due to purity consideration, at least 4 tracks are requested to define proton interactions. Once the vertex points are identified, the algorithm searches for the parent proton track that is closest to the vertex and within a maximum distance of 3μm. The number of vertices inside the tungsten is higher than the vertices inside plastic and emulsion due to the high density of the tungsten.

CHAPTER 5

MEASUREMENT OF PROTON INTERACTION LENGTH

5.1 Proton Interaction Length

The interaction of a single particle with a target material is random. It can not be predicted how far a single particle travels before it interacts. However, the average interaction behavior of many particles can be predicted.

Let us consider a situation to elaborate on this average behavior. Assume a significant number N_0 of identical and energetically same particles incident on a thin layer of the target material with thickness Δx. Passing through the layer, some of the particles interact while some do not. If we define the number of interacting particles as ΔN, then the probability of interaction in the thin layer can be defined as $\frac{\Delta N}{N_0}$. Now, if we measure the number of interacting particles for different thicknesses and plot probability per unit distance, we see that the probability fluctuates a lot as Δx decreases.

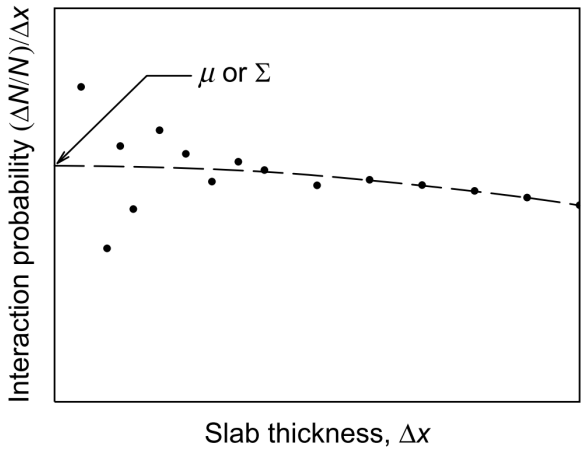


Figure 5.1: Interaction probability per unit distance.

To reduce these fluctuations, we can repeat the experiment several times and take averages for each Δx. As a result, we see fluctuations tend to cancel out and approach a smooth curve, which can be described by a constant μ as in Figure 5.1. This constant can be defined as:

$$\mu \equiv \lim_{\Delta x \to 0} \frac{\Delta N/N_0}{\Delta x} \tag{5.1}$$

is called "linear interaction coefficient"[18].

The exponential behavior of particle reduction is of interest to us. To account for that, let us now consider the case:

The parallel beam of particles is incident on the layer and define the number of particles at $x = 0$ to be $N(0)$. The number decreases due to interactions until depth x. If we consider the non-interacted particles at depth x, i.e., $N(x)$, their number will decrease due to interactions between x and $x + \Delta x$ and become $N(x + \Delta x)$. Then the probability that a non-interacted particle interacts as passing through Δx is:

$$P(\Delta x) = \frac{N(x) - N(x + \Delta x)}{N(x)} \tag{5.2}$$

Taking the limit as $\Delta x \to 0$ and from Eq.(5.1):

$$\begin{aligned} \mu &= \lim_{\Delta x \to 0} \frac{P(\Delta x)}{\Delta x} \\ &= \lim_{\Delta x \to 0} \frac{N(x) - N(x + \Delta x)}{\Delta x} \frac{1}{N(x)} \\ &= -\frac{dN(x)}{dx} \cdot \frac{1}{N(x)} \end{aligned} \tag{5.3}$$

Rearranging Eq.(5.3) we have:

$$\frac{dN(x)}{dx} = -\mu N(x) \tag{5.4}$$

Taking into account the initial condition i.e, at $x = 0$, $N(x) = N(0)$. Then the

solution is:

$$N(x) = N(0)e^{-\mu x} \tag{5.5}$$

Rearranging,

$$\frac{N(x)}{N(0)} = e^{-\mu x} \tag{5.6}$$

The LHS of the Eqn. 5.6 is the survival probability P a particle travels up to distance x. In other words, it is the ratio of remaining particles to the incident particles.

Then the probability that a particle does not interact until x but interacts somewhere between x and $x + dx$ is:

$$\int_0^\infty p(x)dx = (e^{-\mu x})(\mu dx) \tag{5.7}$$

which equals 1 as it should be for a PDF.
Now, if we want to find the average distance $\bar{x}$ traveled by a particle:

$$\begin{aligned} \bar{x} &= \int_0^\infty xp(x)dx \\ &= \mu \int_0^\infty xe^{-\mu x}dx \\ &= \frac{1}{\mu} \end{aligned} \tag{5.8}$$

The average distance traveled before an interaction happens is also called the "mean free path." As seen from Eqn. 5.8, it is inversely proportional to the interaction coefficient.

We can write the survival probability until x in terms of number of interacted particles if we define:

$$N(x) \equiv N(0) - N^{'} \tag{5.9}$$

where $N^{'}$ is the number of interacted particles. So that the Eqn. 5.6 becomes:

$$1 - \frac{N'}{N(0)} = e^{-\mu x} \tag{5.10}$$

Substituting the result of the Eqn. 5.8 into Eqn. 5.10 and taking the natural logarithm of both sides we have:

$$\bar{x} = -\frac{x}{\ln\left(1 - \frac{N'}{N(0)}\right)} \tag{5.11}$$

The mean free path describes the distance traveled before any interaction(such as nuclear, scattering, and so on) happens. However, we are interested in the "hadronic" interaction of protons. In other words, the interaction protons do with the nucleons of the target material and creating other hadrons as a result. Thus, to be specific, we use the notation λ instead of $\bar{x}$ to account for "hadronic interaction length." Further, since in the experiment, we are measuring the number of interacted protons that are incident on the tungsten, x can be changed into the thickness of tungsten, i.e., L.

$$\boxed{\lambda = -\frac{L}{\ln\left(1 - \frac{N'}{N(0)}\right)}} \tag{5.12}$$

5.1.1 The Measurement

The module PD05 from the 2018 run is used for the measurement. The last two tungsten plates are not included in the analysis due to the low efficiency of the corresponding data. The EPOS event generator is used for the efficiency estimations and comparison with the data.

By applying proton-linking to the linked-tracks files, TrackID's before and after each tungsten are compared and stored in proton-linking files; if a TrackID was present before a tungsten but absent after it, the missing tracks are identified as interacted primary protons inside the tungsten. Then by comparing the number of protons identified in the proton-linking files to the number in the True MC, proton-linking efficiency is estimated. Then, the missing TrackID's are searched within the vertexing file and the vertices associated with these TrackID's are identified as primary proton interaction points. The resolution of the vertex position is 18 μm. Because of that, at the boundaries between tungsten and emulsion, interactions in emulsion may

be mis-reconstructed as being inside the tungsten and vice-versa. Also, thickness of tungstens are not constant in a module. To address these issues, 18 μm cut i.e. acceptance cut is applied at the tungsten-emulsion boundaries(Figure 5.2).

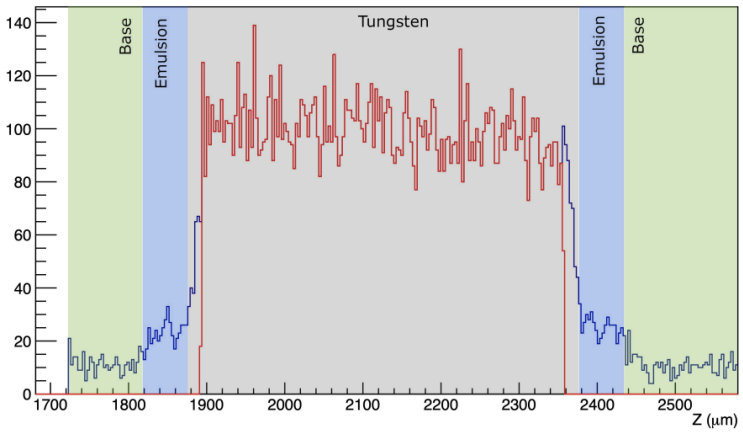


Figure 5.2: Vertex distribution in beam direction. Vertices inside and outside acceptance cut are shown as red and blue lines respectively.

The selected primary interaction points after the acceptance cut are compared with the true primary proton vertices. For this, if Delta-Z of the compared vertices is within the 18 μm and Delta-Transverse is within the 1.8 μm vertex is assumed as a truly reconstructed vertex. Then, by dividing number of truly reconstructed vertices with total number of primary proton interactions in the MC truth, the total efficiency is estimated.

It is recognized that proton-linking efficiency and total efficiency are affected by the track density. Also track densities in MC and data are not the same, so that in a higher track density environment like in the data it is expected to see a lower efficiency. Thus, efficiencies found from MC can not be applied directly to the data. To tackle this issue, efficiencies are parametrized as a function of track density. Resulting linear functions (Figures 5.3 and 5.4) and track densities for data are used to estimate efficiencies for data. The results for MC are given in Table 5.1 and for data in Table 5.2, for both of them total efficiency decreases as downstream.

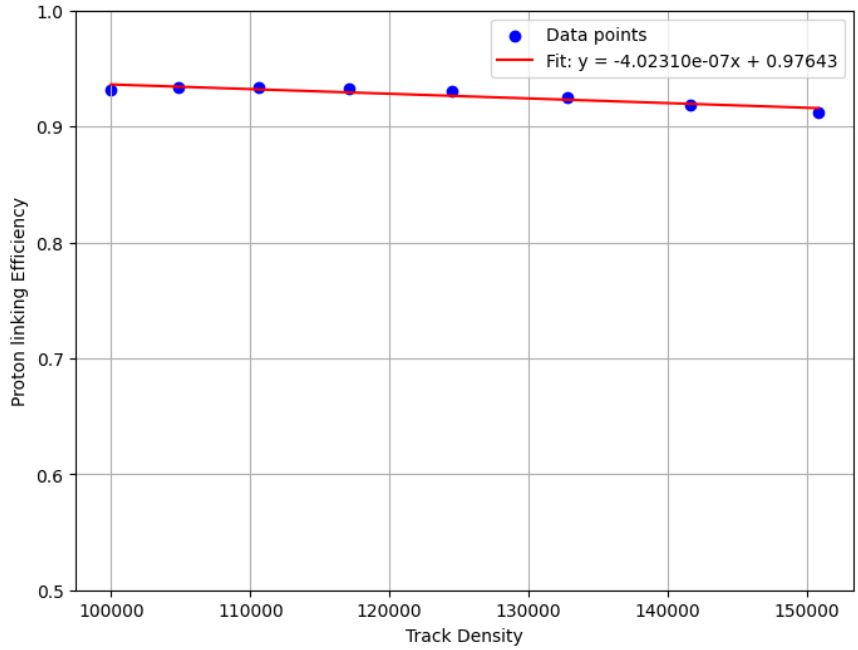


Figure 5.3: EPOS Proton-linking efficiencies as a function of track density.

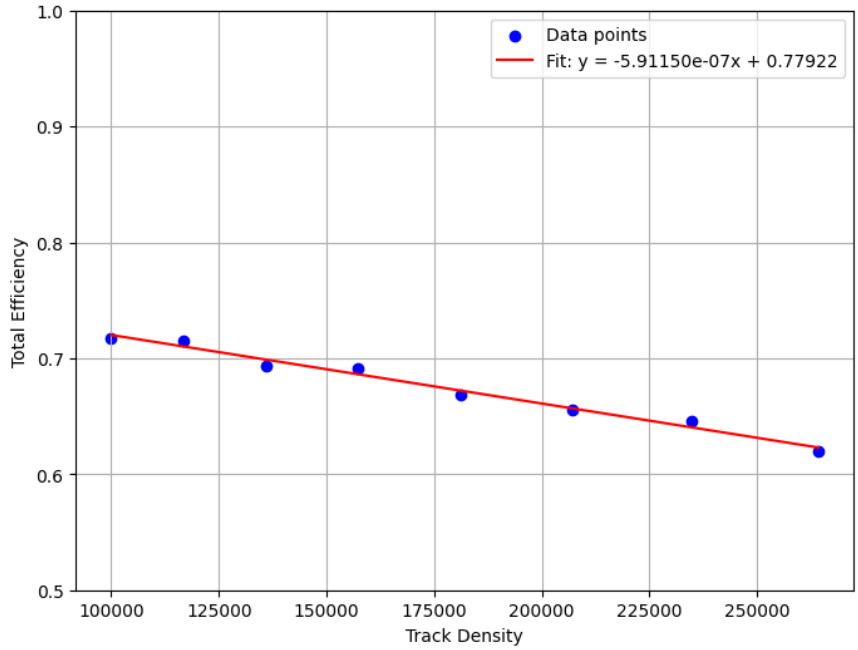


Figure 5.4: EPOS total efficiencies as a function of track density.

Tungsten	Proton-linking Efficiency	Total Efficiency
1	0.936 ± 0.001	0.720 ± 0.025
2	0.934 ± 0.001	0.710 ± 0.025
3	0.932 ± 0.001	0.699 ± 0.025
4	0.929 ± 0.001	0.686 ± 0.025
5	0.926 ± 0.001	0.672 ± 0.025
6	0.923 ± 0.001	0.657 ± 0.025
7	0.919 ± 0.001	0.640 ± 0.025
8	0.916 ± 0.001	0.623 ± 0.025

Table 5.1: EPOS proton-linking and total efficiencies obtained from linear fit, including errors.

Tungsten	Proton-linking Efficiency	Total Efficiency
1	0.936 ± 0.001	0.720 ± 0.025
2	0.934 ± 0.001	0.709 ± 0.025
3	0.931 ± 0.001	0.696 ± 0.025
4	0.928 ± 0.001	0.680 ± 0.025
5	0.925 ± 0.001	0.663 ± 0.025
6	0.922 ± 0.001	0.646 ± 0.025
7	0.918 ± 0.001	0.625 ± 0.025
8	0.914 ± 0.001	0.601 ± 0.025

Table 5.2: Data proton-linking and total efficiencies obtained from linear fit, including errors.

In total, 95,314 primary proton interactions are found in data while 89,121 in MC. For each tungsten, number of incoming primary protons (**N0**), number of interacted primary protons (**N**) calculated and their ratios are shown in the Table 5.3 and Table 5.4 for data and MC respectively.

The interaction length is measured using the Eqn. 5.12 and the Table 5.3 (Table 5.4) for data (MC). The thickness (L) of tungsten is 489 ± 0.1 for data and 464 for EPOS. The total efficiencies and proton-linking efficiencies are used to correct number of

Tungsten Plate	N	N0	N/N0 (%)
1	13,586	3,310,658	0.41
2	13,390	3,292,677	0.41
3	12,653	3,256,746	0.39
4	12,256	3,214,141	0.38
5	11,745	3,157,020	0.37
6	11,264	3,082,105	0.36
7	10,645	2,996,099	0.35
8	9,775	2,892,348	0.34
Total	95,314	25,201,794	0.38

Table 5.3: The number of interacted protons (N) and the number of incoming protons (N0) for each tungsten and their ratios (Data).

Tungsten	N	N0	N/N0 (%)
1	12,185	3,259,305	0.38
2	11,947	3,238,152	0.37
3	11,695	3,212,088	0.36
4	11,477	3,182,037	0.36
5	11,143	3,146,774	0.35
6	10,762	3,105,149	0.35
7	10,194	3,057,856	0.33
8	9,718	3,000,432	0.32
Total	89,121	25,201,793	0.35

Table 5.4: The number of interacted protons (N) and the number of incoming protons (N0) for each tungsten and their ratios (EPOS).

protons and proton interactions inside the tungsten plate. The number of incoming protons (N_0) is divided by proton-linking efficiency, while number of interacted protons (N) is divided by total efficiency. The results are given in Table 5.5.

Tungsten	Data(mm)	MC(mm)
1	91.4 ± 2.4	95.2 ± 2.5
2	91.0 ± 2.4	95.4 ± 2.5
3	93.7 ± 2.5	95.3 ± 2.5
4	93.7 ± 2.5	94.8 ± 2.5
5	94.0 ± 2.5	94.9 ± 2.5
6	93.5 ± 2.5	95.0 ± 2.5
7	93.4 ± 2.5	96.7 ± 2.6
8	95.0 ± 2.5	97.2 ± 2.6
Mean	$\mathbf{93.2 \pm 2.5}$	$\mathbf{95.6 \pm 2.5}$

Table 5.5: Proton interaction length in tungsten as estimated for Data and EPOS.

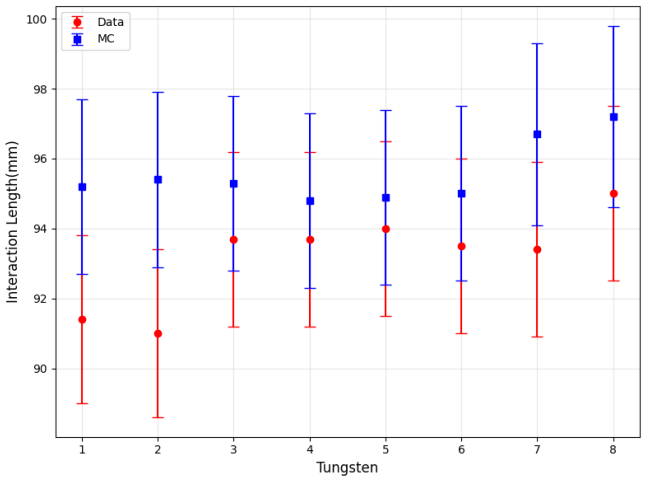


Figure 5.5: Comparison of interaction length for Data and EPOS.

CHAPTER 6

CHARM PAIR SEARCH IN THE PILOT RUN DATA

6.1 Decay Search

A decay search algorithm is applied to the identified vertices, aiming to detect events that topologically resemble those of short-lived particles. The selection criteria are as follows[19]:

- **Charged Particle Decays (1-prong, 3-prong):**
  - Parent particle must be observed in at least two emulsion films.
  - Parent's flight length should not exceed 10 mm.
  - Decay must occur outside the tungsten plate.
  - Parent's angle $\tan\theta \leq 0.3$
  - Daughter's angle $\tan\theta \leq 0.5$
  - $0.01\,\text{rad} \leq \Delta\theta \leq 0.5\,\text{rad}$ where $\Delta\theta$ is the angle difference between the parent and the daughter
  - $10\,\mu\text{m} \leq$ Impact Parameter $\leq 500\,\mu\text{m}$ with respect to the primary vertex
- **Neutral Particle Decays (2-prong)**
  - Parent's flight length should not exceed 5 mm.
  - Decay must occur outside tungsten plates.
  - Parent's angle $\tan\theta \leq 0.3$
  - Daughter's angle $\tan\theta \leq 0.5$
  - $\Delta\theta \leq 0.3\,\text{rad}$ where $\Delta\theta$ is the angle difference between the parent and the daughter

- $10\,\mu$m $\leq$ Impact Parameter $\leq 300\,\mu$m with respect to the primary vertex
- The opening angle between the two daughters must be ≥ 0.01rad

As mentioned before, 2 charmed hadrons should be produced from a proton interaction due to charm number conservation. It would be better to understand this double charm topology by going through a found event as shown in Figure 6.1: Proton interacted at tungsten, the interaction point referred as the primary vertex (V_{1ry}) and multiplicity (number of charged particles) is 18. Among these, one particle exhibits a kink 3.32 mm away from V_{1ry}. The kink daughter's impact parameter relative to V_{1ry} is 174 μm. Also, a neutral particle decay is identified at 2.20 mm away from the V_{1ry} with an opening angle of 0.132 rad. The coplanarity of these decayed particles is 15.2 and due to that, it is unlikely neutral parent is K_0 since they exhibit two-body decay[10].

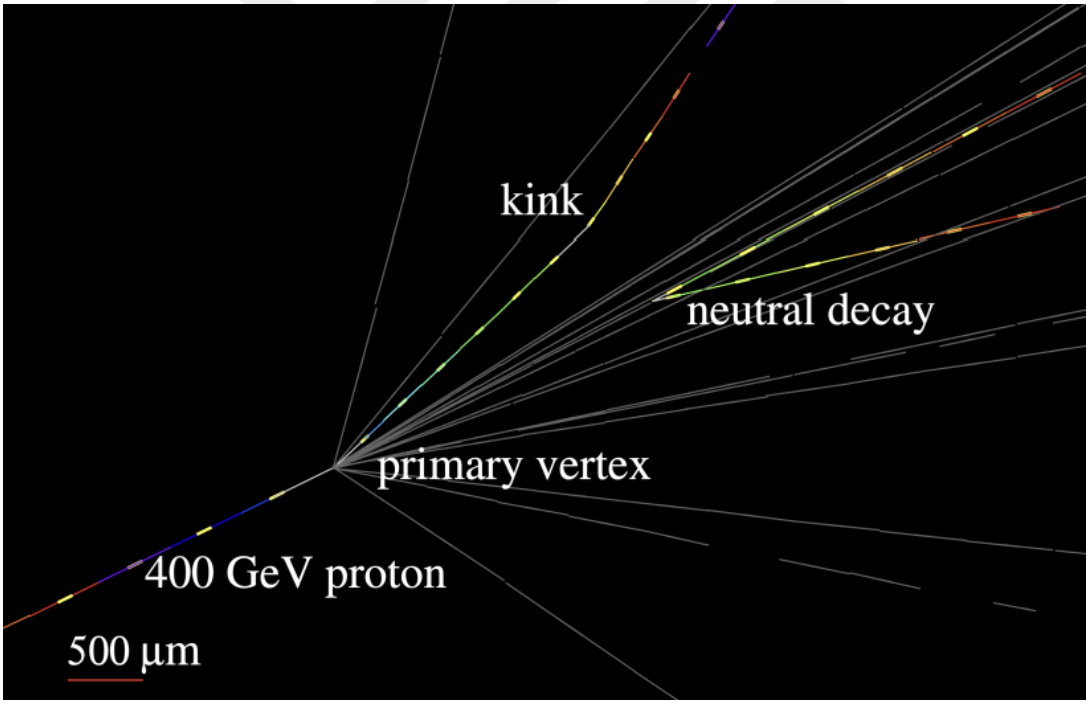


Figure 6.1: Double charm topology example.

6.2 Search For Charmed Hadrons Decaying Into Multi-Prongs

In p-A interactions, charmed hadrons are produced in addition to other hadrons, and due to charm number conservation, they should be produced in pairs. charmed hadrons have short lifetimes of around 10^{-12} s and decay to produce secondary particles.

In the experiment, to simulate 400 GeV p-A interactions, PYTHIA6 [20] and GEANT4 [21] are used for the detector response. The output of these simulations is stored in ROOT files and referred to as "raw" or “truth” files. Further, the reconstruction processes, as mentioned in Chapter 4, such as base-track reconstruction, alignment, and volume-track reconstruction, are applied to these truth files, producing files called "linked tracks". Since the focus of the charm analysis lies in the production of charmed particles from primary beam protons, proton linking is applied. Separate from proton linking, vertexing and decay search algorithms are also applied to linked tracks. Using the outputs of proton linking and decay search, reconstructed ROOT files for each sub-volume are created (Figure 6.2). These are referred to as "reco" files and contain decay vertices and daughter tracks originating from these vertices.

The charmed particles originating from primary interactions and their decays are inspected in the analysis to evaluate the efficiency of the whole reconstruction process, especially decay search, applied to experimental data. Since the same reconstruction process is applied to MC and truth information is fully available in MC truth files, we can estimate the efficiency by comparing reconstructed MC values with MC truth ones.

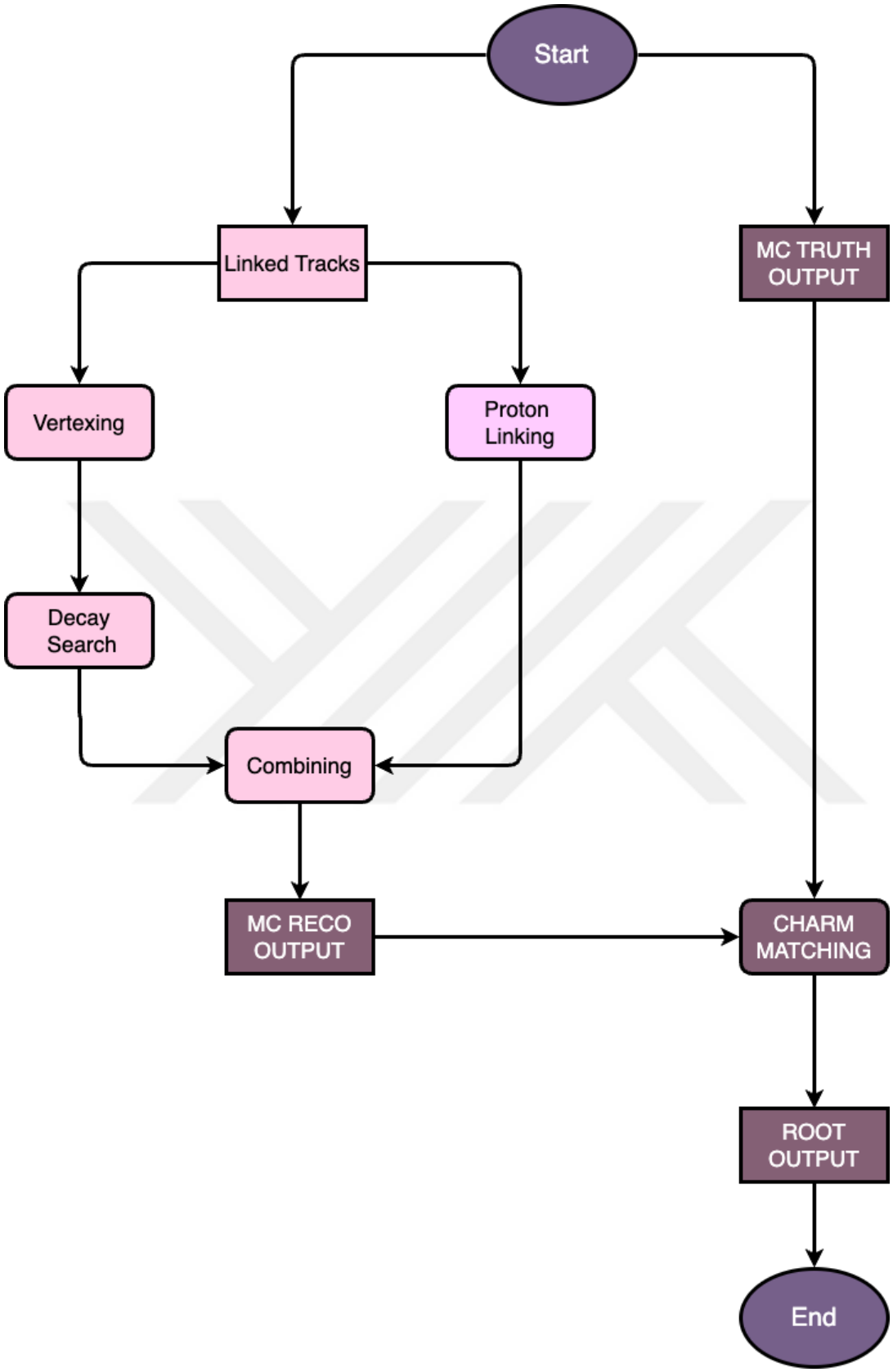


Figure 6.2: Flowchart of Charm Matching.

6.2.1 Reconstructed vs Truth MC Comparison

There are 63 files corresponding to each sub-volume of a module, 8×63 files in total for MC truth, while 8 files for MC reco. First, the algorithm starts with reading entries of MC truth, when it encounters decay vertex, starts to read entries of MC reco. When it encounters any decay vertex in the MC reco, the algorithm calculates the z-difference(Δz) and transverse difference($\sqrt{(\Delta x)^2 + (\Delta y)^2}$) between the proton interaction vertex in the MC truth and MC reco associated with these decay vertices. If:

- $\Delta z < 18\mu$m
- $\sqrt{(\Delta x)^2 + (\Delta y)^2} < 1.8\mu$m

then it calculates the flight length of decayed particle for both MC truth and reco. The reason for the applied cuts arises from the results of Δx, Δy and Δz distributions. When we apply Gaussian fit as shown in Figure 6.3, the correctly reconstructed vertices are located within the 4-sigma of the resolutions.

After checking the flight length difference, if:

- $\Delta(\text{FlightLength}) < 100\mu$m

these vertices considered as correctly reconstructed. The reason for the $100\ \mu$m cut for the flight length is as follows: For correctly matched vertices, the maximum distance is 50 microns; beyond this, the vertices are considered as not matched. To calculate the flight length, we need two vertices: one where the particle was created and one where it decayed, thus requiring a total of 100 microns.

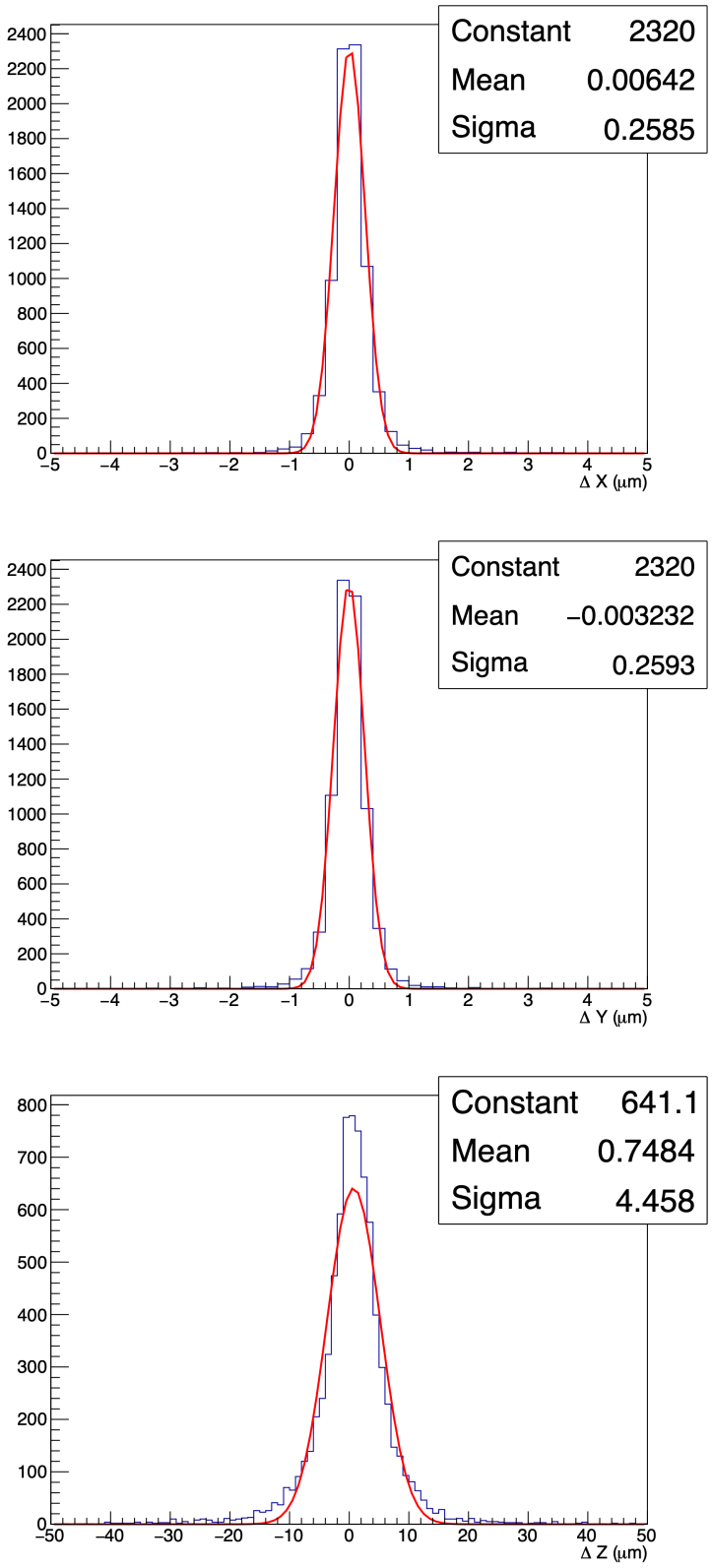


Figure 6.3: Difference in X,Y and Z positions for MC truth and reco.

6.2.2 Decay Search Efficiency Estimation

The results are categorized with respect to number of matched decayed charmed particles. If an event in MC truth is correctly reconstructed in MC reco with respect to Δz, $\sqrt{(\Delta x)^2 + (\Delta y)^2}$ and Δ(FlightLength), it is necessary to further verify the following in the corresponding MC reco:

- Number of decayed charms
- PDG ID
- Number of prongs

If all of them are the same, then this event is considered as "golden" event. Conversely, if even one of these three conditions is not met, the event is classified as a "silver" event. Further, this classification allows for the evaluation of reconstruction efficiency within each category. For example, consider true events with three decayed charmed particles. Some of these events are reconstructed in MC reco, and within the reconstructed events, only one of the three charmed hadrons is successfully reconstructed. By dividing the number of reco events with 1 matched charm by the total number of truth events with three charm, the reconstruction efficiency for the "1 in 3" case can be calculated. Similarly, this process can be repeated for other cases. In the Table 6.1, these reconstruction efficiencies are given.

# of Charm Decay per True Event	# of Charm Decay per Reco Event	# of Total True Events	# of Total Reco Events	Efficiency %
3	1	50415	6747	13.4
3	2	50415	183	0.36
3	3	50415	0	0
2	1	402055	108123	26.9
2	2	402055	7537	1.87
1	1	5341	2166	40.6

Table 6.1: Reconstruction efficiencies for different cases.

The highest reconstruction efficiency, 40%, is observed in the "1 in 1" case. The next highest reconstruction efficiency, 26.9%, is observed in the "1 in 2" case. Efficiency

decreases as the number of decayed charms per true and reco events increases. This is expected because probability to fully reconstruct a multi charm decay event is dependent on correct reconstruction of single charms in that event. Thus, the reconstruction efficiency of the higher number of charm decay events is lower. "1 in 1" and "2 in 2" i.e golden cases can be further classified based on the topologies and efficiencies can be calculated for each topology. In the Table 6.2 and Table 6.3, efficiencies for "1 in 1" and "2 in 2" cases are given respectively. The tables do not include all particles and prongs; the listed topologies are for the the most commonly occurring ones. The events including $\bar{\Omega}_c^0$, $\bar{\Xi}_c^+$, $\bar{\Xi}_c^0$ are excluded since their numbers are too low. "C" stands for charged charmed particle while N for neutral charmed particle and the numbers next to them gives the number of daughters resulting from decay of these particles i.e "prongs" . For the "1 in 1" case, the highest reconstruction efficiency, 28.2%, is observed for N2 with the particle D^0. We are interested mostly in "2 in 2" case, since it is expected to observe D_s mesons with an accompanying charmed hadron. However, there is no D_s observed in "2 in 2", they are observed in "1 in 3" case. For "2 in 2", efficiencies are rather low and the highest efficiency, 3.28% is observed for C_1N_2 topology with D^+ and $\bar{D}^0$ mesons. The efficiencies for Λ_c baryons are quite low but this can be due to MC truth itself, since it is observed that Λ_c production in PYTHIA6 is more than it should be.

Topology	Particle	# of Total Reco Events	# of Total True Events	Efficiency %
C_1	D^+	270	1524	17.7
	D^-	65	559	11.6
	Λ_c^+	40	739	5.41
	$\bar{\Lambda}_c^-$	6	84	7.14
C_3	D^+	314	2660	11.8
	D^-	66	915	7.21
	Λ_c^+	91	2008	4.53
	$\bar{\Lambda}_c^-$	12	251	4.78
N_2	D^0	752	2668	28.2
	$\bar{D}^0$	235	1316	17.9
N_4	D^0	217	1134	19.1
	$\bar{D}^0$	64	508	12.6

Table 6.2: Reconstruction efficiencies for "1 in 1" case.

Topology	Particle	# of Total Reco Events	# of Total True Events	Efficiency %
C_1N_2	$D^+\ \bar{D}^0$	675	20554	3.28
	$D^-\ \bar{D}^0$	348	14518	2.40
	$\Lambda_c^-\ \bar{D}^0$	12	805	1.49
	$\Lambda_c^+\ \bar{D}^0$	57	17058	0.334
C_1N_4	$D^+\ \bar{D}^0$	203	8306	2.44
	$D^-\ \bar{D}^0$	97	6037	1.61
	$\Lambda_c^-\ \bar{D}^0$	1	322	0.311
	$\Lambda_c^+\ \bar{D}^0$	16	6763	0.237
C_3N_2	$D^+\ \bar{D}^0$	582	34269	1.70
	$D^-\ \bar{D}^0$	375	24428	1.54
	$\Lambda_c^-\ \bar{D}^0$	19	2173	0.874
	$\Lambda_c^+\ \bar{D}^0$	199	45817	0.434
C_3N_4	$D^+\ \bar{D}^0$	194	13869	1.40
	$D^-\ \bar{D}^0$	118	9953	1.19
	$\Lambda_c^-\ \bar{D}^0$	6	874	0.686
	$\Lambda_c^+\ \bar{D}^0$	45	18439	0.244

Table 6.3: Reconstruction efficiencies for "2 in 2" case..

Topology based efficiencies with respect to energy for "2 in 2" case are given in the Figures 6.4 , 6.5 , 6.6 , 6.7 for the topologies C_1N_2, C_1N_4, C_3N_2, C_3N_4 respectively. For all four histograms, the efficiencies tend to increase at higher energies. However, the uncertainty also increases because the statistics are lower at higher energies, leading to an increase in the statistical error.

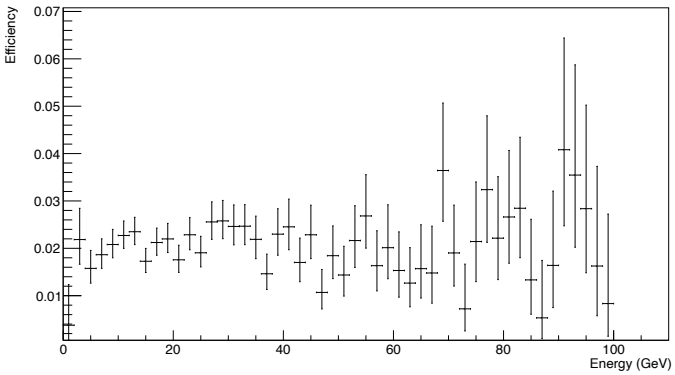


Figure 6.4: Efficiency histogram with respect to energy for C_1N_2 topology.

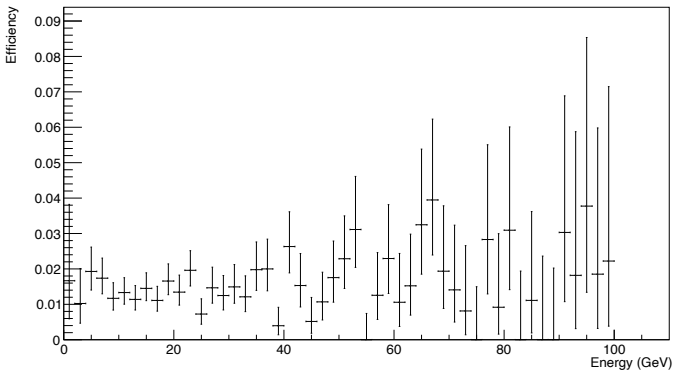


Figure 6.5: Efficiency histogram with respect to energy for C_1N_4 topology.

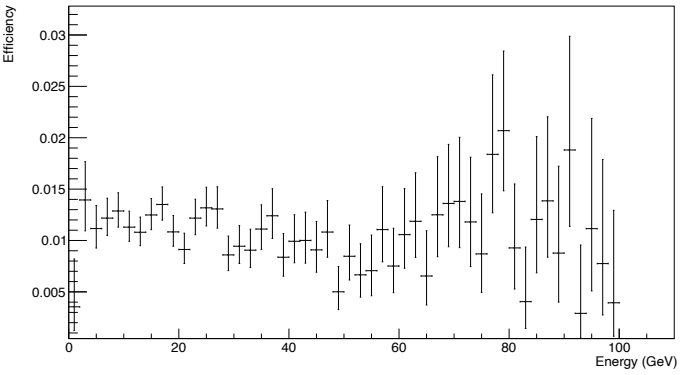


Figure 6.6: Efficiency histogram with respect to energy for C_3N_2 topology.

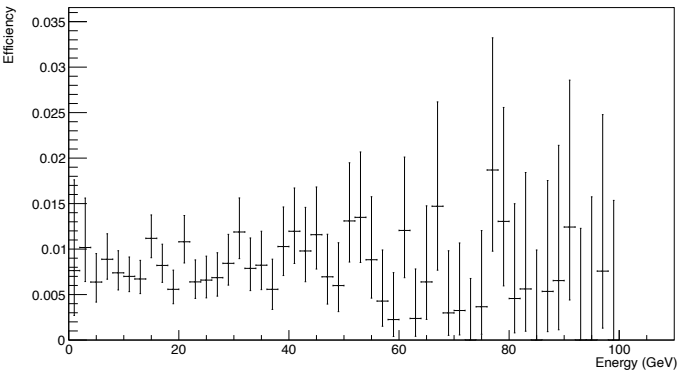


Figure 6.7: Efficiency histogram with respect to energy for C_3N_4 topology.

Events are categorized based on their topology since experimental data does not pro-

vide PDG ID as in the MC. Only the topology of the events can be obtained from the data. This categorization allows for a direct comparison between MC simulation and experimental data. In the experimental data 50 events with C_3N_2 and 6 events with C_3N_4 topology, 56 in total are identified out of 95,314 proton interactions. In Figure 6.8, the flight lengths of charmed hadrons in events with $C_3N_2(N_4)$ and in Figure 6.9 with $C_1N_2(N_4)$ topologies in data and MC are compared. The results show good agreement between the data and MC, indicating consistency between the two distributions. In both cases, the mean flight length in data is higher than in MC. However, when comparing the two topologies, the difference between the mean values for data and MC is more pronounced in $C_1N_2(N_4)$. This offset arises because C_1 corresponds to a kink topology, where misreconstruction is more likely to occur. In kink topologies, when the parent particle is reconstructed together with its decay daughter, leading to potential biases in the reconstructed flight length, especially when resolution effects come into play. On the other hand, C3 corresponds to a trident topology, where the decay products are more independently reconstructed. Since the mean values for data and MC are more comparable in this case, misreconstruction is less probable, leading to better agreement between the two distributions. Additionally, the systematic underestimation of long flight lengths in MC, observed in both cases, could be attributed to:

- Reconstruction inefficiencies, which may affect events with longer flight lengths.
- Track reconstruction challenges in kink topologies, increasing the likelihood of systematic shifts in the reconstructed flight length.

In summary, while overall agreement between data and MC is observed, the larger offset in $C_1N_2(N_4)$ highlights the impact of reconstruction biases in kink topologies, whereas $C_3N_2(N_4)$ shows improved agreement, as expected for a trident topology.

An event with $C_3N_2(N_4)$ topology out of 56 events in data is found in the event display and shown in the Figures 6.10 and 6.11. The proton interacts with the tungsten and one charged and one neutral charmed hadrons are created as a result. The neutral charm doesn't have a track but it has a decay vertex and does two prong decay while the charged one has three prong decay.

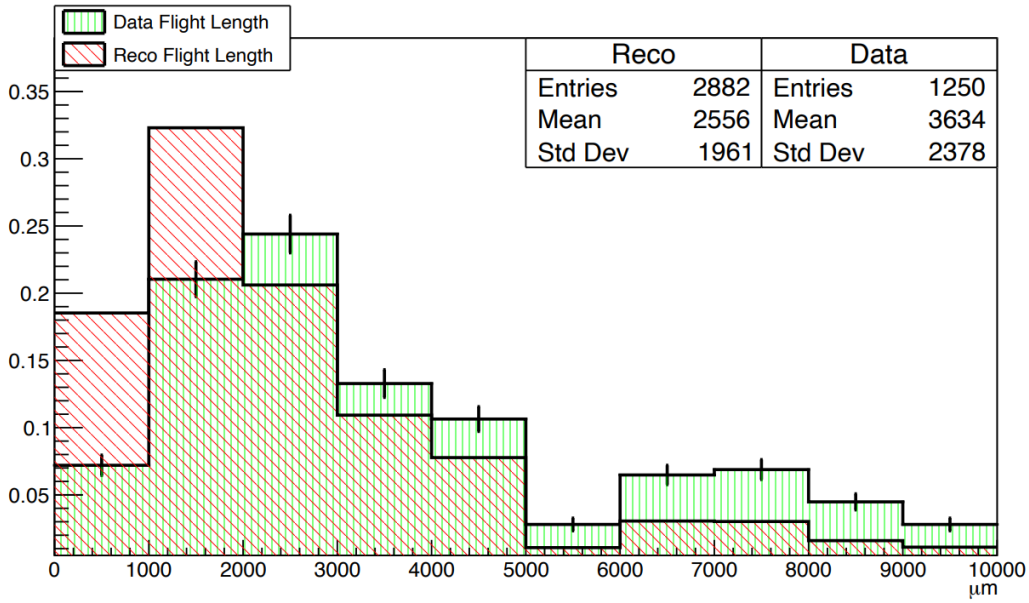


Figure 6.8: Flight length comparison of data and MC for $C_1N_2(N_4)$ topology.

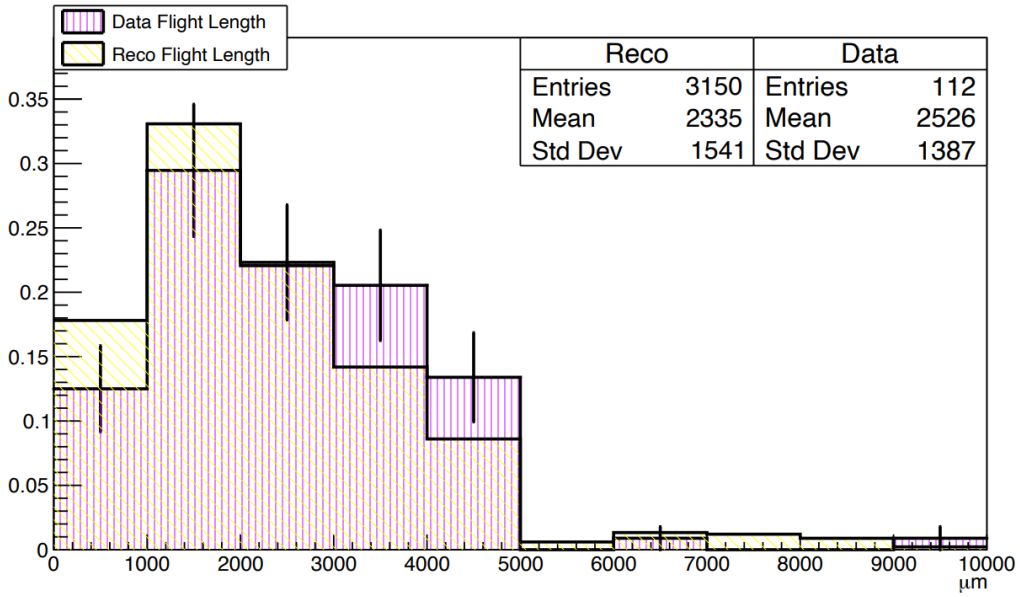


Figure 6.9: Flight length comparison of data and MC for $C_3N_2(N_4)$ topology.

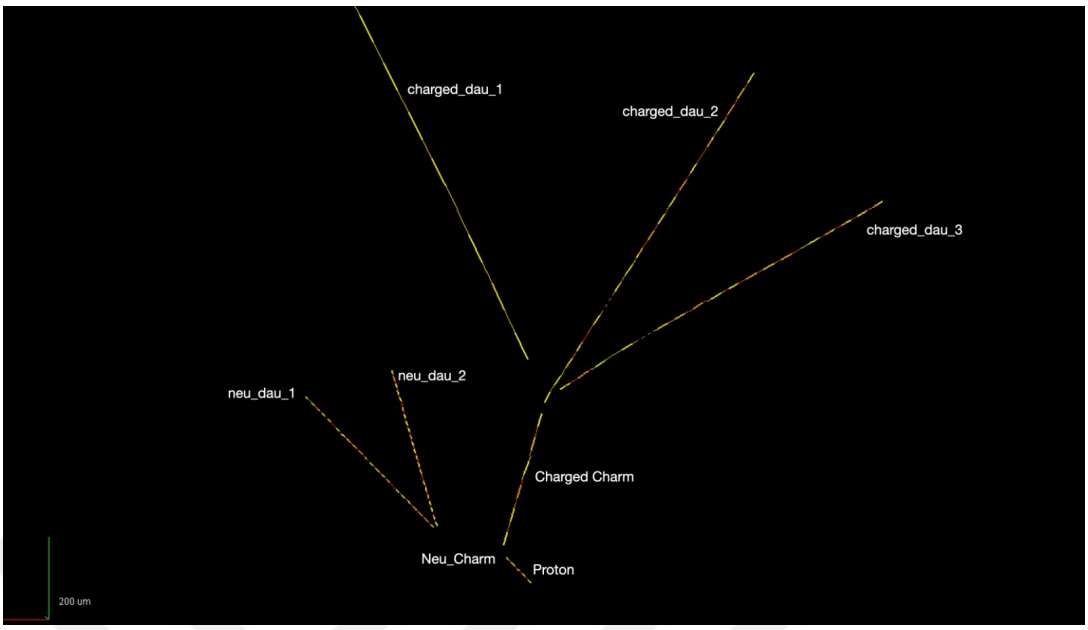


Figure 6.10: An event with $C_3N_2(N_4)$ topology.

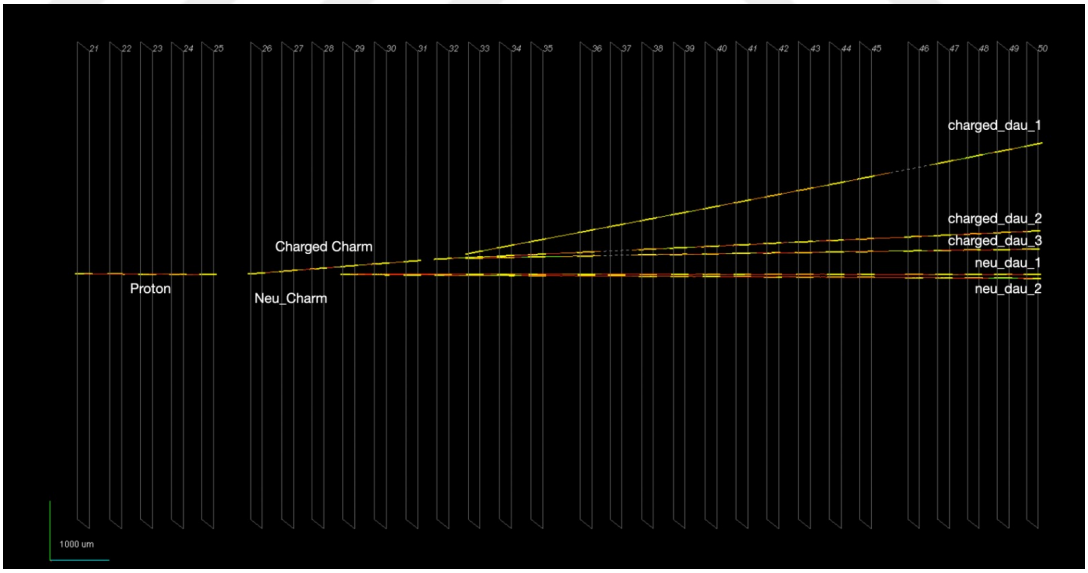


Figure 6.11: An event with $C_3N_2(N_4)$ topology through multiple emulsions in the z direction.

CHAPTER 7

CONCLUSION

This thesis presents the proton interaction length measurement in tungsten and first charm pair search results including multi-prong decays in the DsTau experiment.

The DsTau experiment at CERN focuses on measuring the differential production cross-section of the D_s meson in proton-nucleus interactions at 400 GeV. When protons with 400 GeV of energy interact with tungsten, in addition to other particles, charmed hadrons are also produced. To study and analyze these charmed particles, high-resolution detectors are required, and the DsTau experiment meets this condition through the use of nuclear emulsions. The nuclear emulsion provides sub-micron spatial and a few mrad angular resolution.

This thesis focuses on the measurement of proton-tungsten interaction length and the search for charm pairs in the pilot run data. Using the number of primary proton interactions in each tungsten and the total number of incoming protons, proton interaction length is measured. The mean value of proton interaction length in tungsten is determined to be 93.2 ± 2.5 cm and 95.6 ± 2.5 cm for data and MC respectively which shows a good agreement. Additionally, it is observed the interaction lengths measured remain nearly constant through all tungsten plates in a module, as expected.

In the charm analysis part, correctly reconstructed events are deduced after the matching algorithm is applied. The efficiency of charm reconstruction is estimated for various charmed hadrons and their decay topologies. For each case, reconstruction efficiencies are calculated. The highest reconstruction efficiency is found to be 40% for the "1 in 1" case. The "1 in 1" case refers to events where there is only one true charmed hadron in the event, and that single charmed hadron is successfully recon-

structed. The next highest reconstruction efficiency, 26.9%, is observed in the "1 in 2" case, where an event contains two true charmed hadrons, but only one is successfully reconstructed. A further decrease in efficiency is noted in the "1 in 3" case, where an event has three true charmed hadrons, but only one is reconstructed, resulting in an efficiency of 13.4%. Thus, it can be concluded that reconstructing all the decayed charmed hadrons in an event becomes more challenging as the number of decays increases. The case that we focused on is "2 in 2", where an event contains two true charmed hadrons, both of which are successfully reconstructed has shown a low efficiency of 1.87%. The reconstruction efficiency is plotted as a function of charmed hadron energy. It is observed that efficiencies tend to increase at higher energies. Topology-based classification allows for a direct comparison between MC simulation and experimental data. In total, 56 events with $C_3N_2(N_4)$ and 625 events with $C_1N_2(N_4)$ topology in data are found. The flight length distribution of observed events is compared with MC predictions. It is observed that there is a good agreement in $C_3N_2(N_4)$ topologies between the data and MC. However, the agreement in $C_1N_2(N_4)$ topologies is not good as the multi-prong case. It is due to different signal-to-background ratio in each decay topology. The signal-background ratio is lower in the case of $C_1N_2(N_4)$ decay topology. That gives a poor agreement between the data and the MC. In this thesis a single module of the pilot run data is analyzed to measure the proton-tungsten interaction length and search for the charm pair production. The developed method can be applied to all modules of the pilot run data to increase statistics. High accuracy measurements of charmed hadron pair production in p-A interactions can be achieved when all modules are analyzed.

REFERENCES

[1] Duck, I. & Sudarshan, E. Toward an understanding of the spin-statistics theorem. *American Journal Of Physics*. **66** pp. 284-303 (1998), https://api.semanticscholar.org/CorpusID:121471224.

[2] Goldhaber, M. A Closer look at the elementary fermions. *Proc. Nat. Acad. Sci.*. **99** pp. 33 (2002).

[3] R. Mann, *An Introduction to Particle Physics and the Standard Model*, CRC Press, 2010.

[4] Brown, L., Dresden, M. & Hoddeson, L. Pions to Quarks: Particle Physics in the 1950s. *Physics Today*. **41**, 56-64 (1988,11), https://doi.org/10.1063/1.881136.

[5] Sharma, V. Particle Physics. (https://uou.ac.in/sites/default/files/slm/MSCPH-558.pdf,2022), Course code: MSCPH 558, Uttarakhand Open University.

[6] Close, F. An Introduction to Quarks and Partons. (Academic Press,1979).

[7] Hendry, A. & Lichtenberg, D. The quark model. *Reports On Progress In Physics*. **41** pp. 1707 (2001,2).

[8] Burcham, W. & Jobes, M. Nuclear and Particle Physics. (Addison-Wesley,1995).

[9] Wild, C. Hadroproduction of D mesons in 400 GeV/c p-p interactions. (Durham U.,1987), https://cds.cern.ch/record/180970.

[10] Collaboration, T., Aoki, S., Ariga, A. & Others DsTau: study of tau neutrino production with 400 GeV protons from the CERN-SPS. *Journal Of High Energy Physics*. **2020** pp. 33 (2020), https://doi.org/10.1007/JHEP01(2020)033.

[11] Kodama, K. & [DONuT Collaboration] Observation of tau neutrino interactions. *Physics Letters B*. **504** pp. 218-224 (2001).

[12] Ariga, A., Ariga, T., Lellis, G., Ereditato, A. & Niwa, K. Nuclear Emulsions. *Particle Physics Reference Library*. pp. DOI: 10.1007/978-3-030-35318-6_9 (2020).

[13] Aoki, S. et al. Development of proton beam irradiation system for the NA65/DsTau experiment. (2024), https://arxiv.org/abs/2303.13070.

[14] Morishima, K. & Nakano, T. Development of a new automatic nuclear emulsion scanning system, S-UTS, with continuous 3D tomographic image read-out. *JINST*. **5** pp. P04011 (2010).

[15] Collaboration, T. Description of the Data Processing. (https://twiki.cern.ch/twiki/bin/view/DsTau/DescriptionOfTheDataProcessing,2024), Accessed: December 15, 2024.

[16] Yuksel, E. Study of proton interactions in the DsTau(NA65) Experiment at the CERN-SPS. (Middle East Tech. U., Ankara,2024), https://cds.cern.ch/record/2917039, Presented 03 Oct 2024.

[17] Collaboration, N. Study of Proton-Nucleus Interactions in the DsTau/NA65 Experiment at the CERN-SPS. (2024), https://arxiv.org/abs/2411.05452.

[18] Dunn, W. & Shultis, J. 9 - The Fundamentals of Neutral Particle Transport. *Exploring Monte Carlo Methods*. pp. 235-267 (2012), https://www.sciencedirect.com/science/article/pii/B9780444515759000099.

[19] Aoki, S. et al. DsTau status report. (CERN, 2019), https://cds.cern.ch/record/2668731.

[20] Sjöstrand, T., Mrenna, S. & Skands, P. PYTHIA 6.4: Physics and Manual. *JHEP*. **5** pp. 026 (2006).

[21] Agostinelli, S., Allison, J., Amako, K., Apostolakis, J., Araujo, H., Arce, P., Asai, M., Bagulya, F., Baranov, O., Barnes, R. & Others GEANT4 - A Simulation Toolkit. (http://www.geant4.org/,2003), CERN-W-004, CERN.